Atmospheric Transport Pathways of Oxidized Mercury at Storm Peak Laboratory

A THESIS

Presented to

The Faculty of the Environmental Studies Program

The Colorado College

In Partial Fulfilment of the Requirement for the Degree

Bachelor of Arts in Environmental Science

By

Brandon Chavin Chan

December 2022

Dr. Lynne Gratz

Associate Professor of

Environmental Science, Colorado College

Dr. Rainer Volkamer

Professor of Chemistry,

University of Colorado Boulder & CIRES

Table of Contents

Abstract

Mercury is a global pollutant and neurotoxin that bioaccumulates via the food chain and is harmful to the nervous system. Elemental mercury (Hg^0) is relatively inert in the atmosphere compared to its oxidized state (Hg^{II}). Atmospheric deposition is a major source of mercury to the ecosystem; therefore, atmospheric oxidation makes mercury more bioavailable. This study expands on past work to characterize atmospheric transport regimes of Hg^{II} measured at the continental, high-elevation Storm Peak Laboratory (SPL) in Steamboat Springs (3,220m asl). Hourly-averaged measurements of Hg^0 and Hg^{II}, criteria gases (CO, NO_x, O_3, SO_2), and meteorological measurements from March 12, 2021 to October 10, 2021 and from March 1, 2022 to May 31, 2022 were used to characterize air mass composition and origin at this location. Cluster analysis was applied to hourly 10-day air mass back trajectories, generated using Global Data Assimilation System (GDAS) input meteorology and the Hybrid Single Particle Lagrangian Integrated Transport (HYSPLIT) model. Trajectories were initiated from the location of SPL (40.455°N, 106.744°W) with a starting height of 1000m AGL, determined to closely represent the typical atmospheric pressure at the lab (675 mb). Cluster output was merged with the hourly measurement data to determine if concentrations of Hg^0, Hg^{II}, and other trace gases were statistically different between transport regimes and by season. The back-trajectories showed prevailing westerlies for the measurement periods, consistent with previous analyses of local wind measurements at SPL. In spring 2021, the highest mean concentration of Hg^{II} was associated with northerly transport from continental Canada as well as transport from the north-central Pacific, whereas in both spring 2021 and 2022 trans-Pacific transport was associated with comparably high levels of Hg^{II}. These clusters also had the lowest mean concentrations of Hg^0, consistent with oxidation chemistry as a source of Hg^{II} measured at SPL. For the summer and fall periods, the highest mean Hg^{II} concentrations were associated with shorter distance westerly transport. Across all seasons, enhanced Hg^{II} concentrations occurred in dry air masses suggestive of free tropospheric origin, and similar transport patterns were found consistent with past research at high-elevation sites.

1. Introduction

Mercury (Hg) is a globally distributed hazardous neurotoxin that enters the atmosphere through natural and anthropogenic means. Naturally, mercury enters the atmosphere by sources such as biomass burning and volcanic activity. Mercury is also released to the atmosphere by the burning of fossil fuels and waste. The increase of industrial activity has altered the natural cycling of mercury, increasing Hg concentrations in the atmosphere (Pavithra et al., 2023). Elemental mercury (Hg^0) is relatively inert in the atmosphere compared to its oxidized state (Hg^{II}), which is more water soluble and bioavailable. The atmosphere is a reservoir of mercury, and the main way mercury enters ecosystems is through atmospheric deposition. Mercury can exchange between reservoirs and enter ecosystems, where it can be methylated in the aquatic environment and bioaccumulate (Lyman et al., 2020).

The anthropogenic emission of mercury to the environment has been a pressing public health concern for several decades. For example, in May 1956, people living in Minamata, a city in Japan’s Kyushu Island, were discovered to have been poisoned by methylmercury as a result of ingesting fish and shellfish contaminated with methylmercury discharged in wastewater from a chemical plant (Harada, 1995). Symptoms of this disease (Minamata disease) include ataxia, dysarthria, and sensory constrictions. The chemical plant, Chisso Corporation, did not stop its contamination until 1968, leading to many deaths. There are many other examples where the inhalation during industrial processes or through spills and digestion of mercury have caused damage to organs and the nervous system in humans (WHO, 2022).

In addition to impacts on human health, elevated mercury levels have also impaired the health of animals and ecosystems. For example, one study measured Hg concentrations in bird feathers and found endocrine disruption, impaired ability to accumulate fat for migration, and reproductive issues in the birds with elevated Hg concentrations (Branco et al., 2022). Such harm to ecosystems begins when the process of methylation turns inorganic mercury, which comes from atmospheric deposition, to organic mercury. Then, bioaccumulation can occur in food webs, which can then affect human and ecosystem health. Understanding atmospheric transport regimes will help inform the bioavailability and introduction of Hg to ecosystems.

Emissions policy have helped reduce anthropogenic Hg emissions in the atmosphere. In 1963, the United States’ Clean Air Act was established, and in 1990 amendments were made, establishing Hg as a Hazardous Air Pollutant (HAP) and helping to reduce gas phase trace element emissions including Hg by 49-68% (Gingerich, 2019; LaCount et al., 2021). Mercury is also a global pollutant with globally distributed emissions sources, and there have been international efforts as well to curb this release of Hg. The Minamata Convention was adopted in 2013 by 139 parties to ban new mercury mines, phase-out existing ones, mitigate mercury use in various products and processes, control atmospheric and aquatic emissions, and regulate artisanal and small-scale gold mining, which is a source of Hg emissions (Bank, 2020).

The main reservoirs of Hg are terrestrial soil and marine ecosystems (1,450 and 280 GT, respectively), while the atmosphere only holds ~5 GT Hg (Obrist et al., 2018). However, even though the atmosphere holds considerably less Hg, it is a key component in Hg cycling as previously described (Driscoll et al., 2013).

Elemental Hg accounts for much of Hg emissions to the atmosphere from geogenic and biomass burning sources, as well as from re-emissions from the ocean, while anthropogenic emissions can release both Hg^0 and Hg^{II} in both particle and gaseous forms (Driscoll et al., 2013, Figure 1). In the atmosphere, Hg^0 is usually well-mixed in the boundary layer, and Hg^{II} has been observed to increase in concentrations at higher altitudes, in the free troposphere (FT) (Fäin et al., 2009). Elemental mercury can be transported on continental scales because it is not very soluble and relatively inert; though it can be removed by particle and gas-phase dry deposition or by precipitation, it can also be transported over long distances before being converted to Hg^{II} by chemical oxidation (Pan et al., 2008). While the atmospheric residence time of Hg^0 can extend to several months to a year, Hg^{II} has a much shorter residence time due to its high reactivity and water solubility. Therefore, once atmospheric Hg is in its oxidized form, whether by emission or chemistry, it tends to deposit relatively quickly.

There are several hypotheses based on observational, experimental, and theoretical evidence for the complex chemistry and fate of atmospheric Hg^{II}. Some earlier studies suggested that ozone (O_3) and the hydroxyl radical (OH) were the main oxidants of Hg (Calvert and Lindberg, 2005), but later studies indicated that these reactions are unlikely under thermodynamic and kinetic constraints of the atmosphere (Driscoll et al., 2013). Some studies show that Hg is oxidized in the FT by halogens like bromine (Br) (Coburn et al., 2016; Gratz et al., 2015; Swartzendruber et al., 2006; Wang et al., 2015). Recent studies have revisited the role of OH as the oxidant, followed by O_3 as a secondary oxidant in the process of mercury oxidation (Castro et al., 2022). The overall oxidation reaction is an exothermic process (Shah et al., 2021):

$$\mathrm{Hg}^{0} + Y + \mathrm{M} \rightarrow Y\mathrm{Hg}^{\mathrm{I}} + \mathrm{M} \tag{1}$$

$$Y\mathrm{Hg}^{\mathrm{I}} + \mathrm{Z} + \mathrm{M} \rightarrow Y\mathrm{Hg}^{\mathrm{II}}\mathrm{Z} + \mathrm{M} \tag{2}$$

$$Y\mathrm{Hg}^{1} + \mathrm{Z}_{1} \rightarrow \mathrm{Hg}^{0} + Y\mathrm{Z}_{1} \tag{3}$$

where Y is a radical (Br, Cl, OH), which form weakly bound intermediates, $Y\mathrm{Hg}^{\mathrm{I}}$. M is a non-reactive molecule, and Z ≡ OH, Br, NO_2, HO_2, BrO, ClO. $Y\mathrm{Hg}^{\mathrm{II}}\mathrm{Z}$ is formed by the addition of another radical (Figure 2).

As a globally distributed pollutant, the oxidation chemistry of Hg in different environments is poorly understood. Ongoing studies have been conducted at mountaintop sites, where there is less influence from ambient sources, better access to the FT, and easier decoupling of boundary layer processes from those in the FT to study Hg transport regimes and the chemical cycling between Hg^{0} and $\mathrm{Hg}^{\mathrm{II}}$ (Timonen et al., 2013). For example, a study at Mt. Observatory (MBO), Oregon revealed elevated $\mathrm{Hg}^{\mathrm{II}}$ concentrations and an anticorrelation between Hg^{0} and $\mathrm{Hg}^{\mathrm{II}}$ during Asian long-range transport events (Timonen et al., 2013). Timonen et al. (2013) also observed highest $\mathrm{Hg}^{\mathrm{II}}$ values in the FT, where subsidence is suggested to drive $\mathrm{Hg}^{\mathrm{II}}$ levels (Amos et al., 2012). Another study looked at the chemical cycling and spatiotemporal distribution of Hg in the atmosphere at Storm Peak Laboratory (SPL), Colorado (Fäin et al., 2009), where enhancements of reactive gaseous mercury (i.e. $\mathrm{Hg}^{\mathrm{II}}$ in the gas phase) measured at the laboratory were found not to be induced by pollution events but from the oxidation of Hg^{0}. Besides the need for more understanding on the mechanisms and the associated kinetics of oxidation pathways, one reason for the uncertainty of atmospheric Hg chemistry comes from the limitations in measurement techniques. Past studies have relied on a potassium chloride (KCl) denuder-based system to measure $\mathrm{Hg}^{\mathrm{II}}$ species, but concentrations are frequently underestimated using this method (Gustin et al., 2021).

In this study, we utilized a dual-channel Hg measurement system that more accurately quantifies $\mathrm{Hg}^{\mathrm{II}}$ to conduct a multi-season study of ambient Hg at SPL. We used the Hybrid Single Particle Lagrangian Integrated Transport (HYSPLIT) model to examine transport regimes of air masses measured at SPL. Along with the HYSPLIT model results, we used chemical and meteorological measurements at SPL to inform air mass characterization of larger-scale transport, cycling, and chemistry of Hg in a continental atmosphere.

2. Methods

2.1 Site Description

Storm Peak Laboratory (SPL) is a continental, permanent mountain-top research facility in Steamboat Springs, CO (3220 m M.S.L.; 40.455 N, 106.744 W). SPL is located on a 70km long north-south mountain barrier, receiving prevailing westerly winds. The laboratory is about 1150m above Steamboat Springs, allowing it to receive relatively clean air from its surroundings. The elevation and the distance from major pollution centers allow for measurements within the free troposphere as the local boundary layer height shifts (Obrist et al., 2008). SPL has been in operation for nearly 30 years (https://atmos.utah.edu/storm_peak_lab/index.php), serving research projects that can have a longer-term studying period, with instruments measuring meteorology, criteria and trace gases, and aerosol properties.

2.2 Mercury Instrumentation and Data Collection

Atmospheric Hg^0 and Hg^{II} were measured from March 13, 2021 to October 11, 2021, and from March 3, 2022 to September 30, 2022. For the purpose of this analysis, only data until May 31, 2022 was used. The Utah State University dual-channel system with a Tekran 2537X analyzer operates by pulling a sample of ambient air, which enters the main inlet at a rate of 8 standard L minute^{-1}, into a front-unit weatherproof box (Figure 3). This box, the dual-channel system, houses a pair of cation-exchange membranes which are situated in series with one another and a pyrolyzer (Zwecker, 2021). The pyrolyzer, maintained at 650°C, converts all Hg^{II} to Hg^0 such that the analyzer measurement reflects total Hg ($THg = Hg^{II} + Hg^0$) (Lyman et al., 2020). In contrast, the cation-exchange membrane removes Hg^{II} from the air stream and allows Hg^0 to pass through. In so doing, the analyzer measurement reflects only Hg^0. Oxidized Hg is calculated by taking the difference between THg and Hg^0. A valve switches between the pyrolyzer and membrane channel every five minutes, resulting in a complete set of measurements every 10-minutes. Inlet and sample lines are maintained at a temperature of 110°C to reduce contamination and wall losses.

With a supplemental pump, the Tekran 2537X analyzer maintains constant sample flow at a rate of 1 standard L m^{-1}. Sampled air passes over one of two gold traps, which collect Hg^0 on a 2.5-minute interval. The Tekran 2537X measures Hg concentration by multiplying the maximum peak height by a calibration factor and dividing it by the sample flow rate of the analyzer (Lyman & Jaffe, 2012). Hg^0 and Hg^{II} measurements are expressed in mass concentrations, ng m^{-3}and pg m^{-3}, respectively.

Routine maintenance of the dual-channel system at SPL during this study included changing the soda lime trap to remove reactive gases and protect gold traps. This and changing the cation exchange membranes were done on a biweekly basis. The inlet glassware was replaced each month. Internal, automated calibrations of the Tekran 2537X occurred every 71 hours. Mercury vapor injections on the Tekran 2537X were performed every 6-8 weeks to verify the internal 2537X calibration source's permeation rate.

There were several time periods where data were not available due to instrument or operator error. The main flush pump failed and was offline from May 12, 2021 to June 6, 2021. Due to instability in the 2537X UV lamp that affected the accuracy of Hg peak detection, data from June 29 –July 9, 2021 were removed. A blockage in the cation exchange membrane from August 2-10, 2021 also led to unavailable data. Unavailable data for the 2022 spring data include March 1, 2021 to March 3, 2021, as well as gaps ranging from one to multiple hours due to calibrations.

The dual-channel system also includes an automated Hg calibration system to verify precision of measurements over time. Calibrating for both Hg^{II} and Hg^0 is a key improvement to Hg^{II} measurements and an objective of the study (Gustin et al., 2015; Jaffe et al., 2014). The calibrator operates by injecting known concentrations of gaseous Hg^0, $HgBr_2$, and $HgCl_2$ into the inlet of the instrument at pre-programmed time intervals. The calibrator was installed at SPL in July 2021, and calibrations were run on a weekly basis during this study. The automated calibrator performance is being evaluated in a separate analysis and will not be shown here.

2.3 Meteorological and Supplementary Chemical Instruments

Meteorological variables (air temperature, relative humidity, barometric pressure, wind speed, and wind direction) were measured concurrently with criteria gases and atmospheric mercury at SPL. The meteorological instruments were situated 10 m above ground level (AGL) at the rooftop of SPL and collected on a 5-minute time resolution. The meteorological data are made publicly available by MesoWest (mesowest.utah.edu). The criteria gas measurements included: ozone (O_3; Thermo Model 49i analyzer; 1 min), nitrogen oxides (NO_x; Thermo Model 42i NO-NO_2-NO_x analyzer; 1 min), sulfur dioxide (SO_2; Thermo Model 43i analyzer; 1 min), carbon monoxide (CO; Teledyne model 300E, 2.5 min), and radon (RAD7 monitor; 10 min), For the springtime, NO_x values more than 3 standard deviations above the seasonal mean were removed due to snowcat passings while the ski resort was in operation. The TSI model 3563 Nephelometer at 550nm was used to measure PM_1 and PM_{10} aerosol scattering. All instrumentation related to the present analysis were run continuously from March 12, 2021 with the exception of CO, for which data collection began on July 9, 2021. Summertime data were also screened for the likely presence of smoke, based on the criteria of $CO \geq 150$ ppb, PM_{10} scattering 35 Mm^{-1} and PM_1 scattering 30 Mm^{-1} for a minimum of 1-hour; however, those data are still included for the purpose of the present analysis. Approximately 30% of summer (June – September 2021) data were determined to be smoky. A future version of this analysis could include re-running the cluster analysis without smoke periods to characterize summertime transport regimes for Hg^{II} and other measurements in the absence of smoke.

2.4 Statistical Analysis

All data were averaged to 1-hour intervals corresponding to the top of each hour. We split each calendar year of data into three seasons. We defined Spring 2021 as March 12-May 31, 2021, Summer 2021 as June 1-August 31, 2021, Fall 2021 as September 1-October 10, 2021, and Spring 2022 as March 1-May 31, 2022. Summary statistics, boxplots, independent samples t-tests, and correlation analyses were computed using a combination of Excel v16.66.1, RStudio 2022.07.1, and IBM SPSS Statistics v28.0.0.0. Significance was considered at p-values < 0.05 in this study.

2.5 HYSPLIT Back Trajectories and Cluster Analysis

To simulate the path of air masses during the measurement period for 2021 and 2022, we generated 10-day (240 hours) back-trajectories starting every hour during the measurement period, using (GDAS) 1°x1° input meteorology and the Hybrid Single Particle Lagrangian Integrated Transport (HYSPLIT) model by the National Oceanic and Atmospheric Administration (NOAA) (HYSPLIT, v4.9, Draxler and Rolph, 2014). The trajectories were initiated from the location of SPL (40.455°N, 106.744°W) with a starting height of 1000m AGL, determined to closely represent the typical atmospheric pressure at the lab (675 mb). In HYSPLIT, we applied cluster analysis to those trajectories, which is produced within HYSPLIT by merging trajectories according to their spatial variance, until the total variance of the individual trajectories about their cluster mean starts to increase (HYSPLIT Tutorial, 2022). Using the total spatial variance graph in HYSPLIT (see figures 4, 8, and 12), the number of clusters is chosen for each season at the point before disparate clusters start to be merged and total spatial variance increases after the leveling-off for remaining iterations (HYSPLIT Clustering Equations, 2022). Based on this approach, six clusters were chosen for Summer 2021 (Figure 13) and Fall 2021 (Figure 17). Seven clusters were chosen for

Spring 2021 and 2022 (Figures 5 and 9). “Time interval (hrs)” and “trajectory skip” were both selected to be 1 on the HYSPLIT menu; this means that HYSPLIT is making the simulation based on data from every hour (endpoint) along the 10-day back trajectory, and including all simulated trajectories from the period. In total, 2,160 backward trajectories were used for Spring 2021, 2,129 were used for Summer 2021, 1,067 for Fall 2021, and 2,198 for Spring 2022. Following the approach of Gratz et al. (2014) where transport regimes of air masses were modeled at MBO to correspond with springtime O_3 and CO measurements, here we merged the hourly measurement data with the hourly trajectories and their assigned cluster number to determine if and how concentrations of Hg and trace gas concentrations differed by transport pathway and season.

3. Results

In this section we summarize the results of the cluster analysis for each individual seasons. In section 4 (Discussion), we draw from these results to highlight the similarities and differences in transport regimes associated with Hg^{II} from one season to another.

3.1 Spring 2021

For Spring 2021 (March 12-May 31, 2021), Figure 5 shows the average trajectory for each of the seven clusters. Cluster 1 depicts the highest mean altitude and represents the fastest trans-Pacific transport of the clusters. Cluster 2 has the second highest mean altitude and second fastest trans-Pacific transport. Cluster 3 is third highest in altitude and represents a transport pathway from the central Pacific. Clusters 4 and 6 are lower in altitude and depict transport pathways from the north-Pacific. Cluster 5 represents a slower transport regime from the west with a lower altitude. Cluster 7 represents the lowest altitude and depicts a slow northerly continental transport regime.

There are 1,387 recorded Hg^{II} measurements in Spring 2021. Clusters 3 and 7 have the highest Hg^{II} means ($\pm 1\sigma$) (93 ± 40 pg m^{-3} and 103 ± 50 pg m^{-3}, respectively) and these means are not significantly different ($p = 0.177$) from one another. The similarity of these two clusters' medians (95 pg m^{-3} and 97 pg m^{-3} respectively) can be seen on the boxplot comparing Hg^{II} by cluster for spring 2021 (Figure 6). Cluster 4 has the lowest Hg^{II} mean at 61 ± 40 pg m^{-3}.

Figure 7 shows the measured hourly Hg^{II} concentrations in Spring 2021, differentiated by color for the associated transport cluster number. Note that early March displays many high Hg^{II} values associated with cluster 5. These high values are shown as the circles above the whiskers for cluster 5 on the boxplot (Figure 6). Much of the data associated with cluster 3 is clustered in time periods typically ranging from two to four days; for example, there is one group of data assigned to cluster 3 around the end of March, and another group end April/early May. On the other hand, much of the data of cluster 7 is distributed throughout the season. In the beginning of April, the Hg^{II} concentration rises, with data mainly assigned to clusters 1 and 2. These and two other periods in Spring 2021 where Hg^{II} concentrations are at least one standard deviation above the seasonal mean for a sustained period are identified as case studies (Derry, 2023) and will be explored in the Discussion section.

In Spring 2021, Hg^{II} is significantly anticorrelated to Hg^0 in all clusters (Table 5). Oxidized Hg is significantly correlated to PM_{10} and PM_1 aerosol scattering in clusters 1, 2, 4, and 6. Oxidized Hg is significantly anticorrelated to WV mixing ratio in clusters 2, 3, 6, and 7. Oxidized Hg is significantly correlated to SO_2 in clusters 2, 3, and 4. Note that SO_2 is a tracer of local combustion (Ahmed et al., 2021) and does not travel long distances on a trans-continental scale due to its short lifetime before being converted to a sulfate ion (Calvert et al., 1985); therefore the correlations between Hg^{II} and SO_2 within the 10-day trajectory clusters here should be interpreted with caution.

3.2 Spring 2022

Like Spring 2021, seven clusters are chosen for Spring 2022 (March 1-May 31, 2022) using the total spatial variance graph in HYSPLIT (Figure 8). Clusters 1 and 2 have similar mean transport regimes with that of clusters 1 and 2 in Spring 2021 and represent the fastest air mass transport in the simulated 10-day period (Figure 9). Cluster 2 in Spring 2022 is on average 1 km AGL lower than cluster 2 in Spring 2021. Cluster 3 depicts a slower, lower altitude transport regime from the Pacific. Cluster 4 has a similar transport regime as cluster 3 in Spring 2021, with transport from the central Pacific. Clusters 5 and 6 are neither the highest or lowest in altitude compared to the other clusters and show faster transport over the Pacific. Cluster 7 of 2022 is similar to cluster 7 in Spring 2021 with a northerly continental transport at lower altitude.

There are 1,695 recorded Hg^{II} measurements in Spring 2022. As shown on the corresponding boxplot (Figure 10), cluster 7 (5% of trajectories) has the lowest median and the least spread. In contrast to cluster 7 in 2021, Cluster 2 has the highest median and maximum Hg^{II}; for mean Hg^{II} concentration, cluster 1 and 2 are not statistically different from each other (p = 0.411). Figure 11 shows the measured hourly Hg^{II} concentrations in Spring 2022, differentiated by color for the associated transport cluster number. Clusters 1 and 2 have the highest Hg^{II} means (85 ± 80 pg m^{-3} and 88 ± 40 pg m^{-3}, respectively), and the lowest Hg means is in cluster 7 at 58 ± 20 pg m^{-3}. Cluster 2, which has the highest Hg^{II} mean, also has the lowest Hg^0, CO, and NO_x means (Table 2).

In Spring 2022, Hg^{II} is significantly anticorrelated to Hg^0, CO, and NOx in all but cluster 7 (Table 6). Oxidized Hg is significantly positively correlated to Hg^0 in cluster 7, which is the cluster with the lowest Hg^{II} mean. Oxidized Hg is significantly anticorrelated with WV mixing ratio in clusters 1, 3, and 7, but is positively correlated in cluster 2. Oxidized Hg is significantly correlated with SO_2 and PM_{10} and PM_1 aerosol scattering in clusters 1, 2, and 3. Oxidized Hg in cluster 7 is significantly correlated to Hg^0, O_3, PM_{10} aerosol scattering, and WV mixing ratio. Oxidized Hg in cluster 6 is significantly correlated to SO_2, PM_1 aerosol scattering, and WV mixing ratio.

3.3 Summer 2021

Six clusters are chosen for Summer 2021 (June 1-August 31, 2021) (Figure 12). Cluster 1 represents a low-altitude northerly continental transport. (Figure 13). Cluster 2 represents a high-altitude transport regime from the Pacific. Cluster 3 depicts a lower-altitude, slower-moving regime from the Pacific. Cluster 4 has the highest mean altitude and has a fast-moving trans-Pacific transport pathway, similar to clusters 1 and 2 in the spring seasons. Cluster 5 is a slow-moving, mid-latitude transport regime from the southwest of SPL. Cluster 6 is a southeast transport regime coming from the direction of the Gulf of Mexico, and this transport pathway was not generated by HYSPLIT for both Spring 2021 and Spring 2022.

There are 1,393 recorded Hg^{II} measurements in Summer 2021. Clusters 3 and 4 have the highest Hg^{II} means and are not statistically different from each other in terms of Hg^{II} ($p = 0.661$). The boxplot (Figure 14) shows many outliers for cluster 5 and it has the second lowest median (108 pg m^{-3}). Cluster 5 also has the second lowest mean at 115 ± 40 pg m^{-3}. Cluster 6 which has the lowest Hg^{II} and CO means have the highest O_3 and WV mixing ratio (7.4 ± 2.2 g/kg) (Table 3).

Figure 15 shows the Hg^{II} concentration in Summer 2021, differentiated by color for the associated transport cluster number. Note that the high Hg^{II} values early in the season are from cluster 5, and Hg^{II} data corresponding to the clusters in general are usually grouped together. For example, most of the data from cluster 6 lies between July 22-August 1, 2021. Four episodes in Summer 2021 will be elaborated on in the Discussion section.

In Summer 2021, Hg^{II} is anticorrelated to Hg^0 and WV mixing ratio in all clusters (Table 7). Oxidized Hg is significantly anticorrelated to NO_x in clusters 3 and 5. Oxidized Hg is significantly correlated to O_3 in clusters 4 and 6. Oxidized Hg is significantly correlated to CO in cluster 5, which has the mostly continental transport pathway from the southwest. No cluster has Hg^{II} data that is either significantly correlated or anticorrelated to aerosol scattering, a difference from all other measured seasons.

3.4 Fall 2021

Six clusters are chosen for Fall 2021 (September 1-October 10, 2021) (Figure 16). Note that the measurement period for Fall 2021 is shorter and thus has less data (960 hours of data) than the other seasons (2208 hours of data for the other three seasons). Cluster 1 represents a low-altitude continental transport regime from the southwest (Figure 17). Cluster 2 depicts a transport regime from the southeast from the direction of the Gulf of Mexico, similar to that of cluster 6 in Summer 2021. Cluster 3 represents a low-altitude transport regime coming from the Pacific, and cluster 4 has a similar transport direction but is higher-altitude and faster-moving. Cluster 5 is similar to cluster 4 with a higher-altitude trans-Pacific transport pathway. Cluster 6 has the highest altitude and depicts a fast transport pathway from the west.

There are 944 recorded Hg^{II} measurements in Fall 2021. Clusters 4 and 5 have the highest Hg^{II} means and are not statistically different from each other ($p = 0.615$) (Table 4). The Hg^{II} means within clusters 3 and 5 are also not statistically different from each other ($p = 0.716$). Note that only seven data points are represented by cluster 6. The boxplot for this season (Figure 18) shows cluster 3 has the largest spread of data. In 2021 Fall, there are values from clusters 1, 2, 3, 4, and 5 that exceeded 0.2 ng m^{-3} (Figure 19). Cluster 6 which does not have data points that exceeded 0.15 ng m^{-3} represents a high-altitude trans-Pacific transport pathway; the other clusters are lower in altitude. Episodes will be identified in the Discussion section. Oxidized Hg is significantly anticorrelated to Hg^0 in clusters 1, 3, and 4 (Table 8). Oxidized Hg is significantly anticorrelated to NOx and WV mixing ratio in clusters 1, 2, and 5, and to CO as well in clusters 1 and 2. Oxidized Hg is significantly correlated to PM_{10} and PM_1 aerosol scattering, and WV mixing ratio in cluster 6. In clusters 3 and 4, Hg^{II} is significantly correlated to O_3 and SO_2 and significantly anticorrelated to aerosol scattering PM_{10} and PM_1. Oxidized Hg is also significantly correlated to O_3 in clusters 1, 2, and 5, and is also significantly anticorrelated to aerosol scattering PM_{10} and PM_1 in cluster 1. Oxidized Hg is significantly correlated to CO in cluster 3.

4. Discussion

Past studies have reported high Hg^{II} concentrations and examined them in relation to concurrently measured trace gases and meteorology at high elevation sites in the western United States, such as at MBO in Oregon (Swartzendruber et al., 2006; Timonen et al., 2013) and at SPL in Colorado (Fäin et al., 2009). Particularly during springtime, trans-pacific transport has been observed at MBO due to ventilation of the East Asia boundary layer and circulation of trans-Pacific plumes (Gratz et al., 2015; Jaffe et al., 2005; Timonen et al., 2013). These studies provide a foundation for further work solidifying the understanding of air mass origins and mercury chemistry. This Discussion will be examining the transport regimes with the aid of relevant past work.

4.1 Springtime Transport Regimes

In Spring 2021, cluster 3 and 7 have the highest Hg^{II} means. They depict a transport regime from the north Pacific and a northerly continental transport regime, respectively. The mean altitude of cluster 3 is around 3000m AGL, while the mean altitude of the northerly continental transport regime stays around 1000m AGL. With the anticorrelation between Hg^{II} and WV mixing ratio, these two clusters indicate that elevated Hg^{II} concentrations are associated with drier air masses. The northerly continental transport regime did not show any significant correlation of Hg^{II} to any of the measured trace gases, suggesting that air masses within cluster 7 were not recently influenced by anthropogenic pollution sources (Fäin et al., 2009). Hg^{II} is significantly correlated to SO_2 in cluster 3 which represents air masses originating over the Pacific 10-days back. However, recent work has shown that upwind power plants west of SPL do not enhance Hg^0 or Hg^{II} (Hoch, 2023). Therefore, the correlation between Hg^{II} and SO_2 may be purely coincidental as westerly winds may pick up SO_2 emissions from the nearby plants, but the simultaneously enhanced Hg^{II} may have a different explanation, such as further upwind source and/or chemistry within the air mass, locally or at a greater distance from SPL (Glasow et al., 2009). Cluster 3's averaged transport pathway also indicates a clockwise loop at about 30° N -150° E. The shape and direction of the trajectory look similar to the type 3 (marine boundary layer) transport in Timonen et al. (2013) and also has low aerosol scattering characteristic of that in Timonen et al. (2013). This transport pathway may suggest an influence by the tropical easterlies at the subtropical high with the prevailing westerlies transporting the air mass to North America.

Both Spring seasons' clusters 1 and 2 are associated with high altitude, long-range transport from the north central Pacific in dry air masses that appear representative of the FT. These two clusters of both spring seasons have similar Hg^{II} means (2021: 80 ± 40 pg m^{-3}, 85 ± 40 pg m^{-3}, 2022: 85 ± 80 pg m^{-3}, 88 ± 40 pg m^{-3}). For Spring 2022, the highest average Hg^{II} concentrations were in these two transport regimes. They also have the lowest seasonal mean water vapor mixing ratios (2.7 ± 2.7 g/kg and 3.0 ± 1.0 g/kg for cluster 1 and 2, respectively, in 2022). For both Spring seasons, Hg^{II} in clusters 1 and 2 are positively correlated to PM_{10} and PM_{1} aerosol scattering. From this, we see that these Springtime transport regimes are similar. These appear similar in origin to the type 2 (anthropogenic events) transport in Timonen et al. (2013) with anticorrelation between Hg^{0} and Hg^{II}. The work of Timonen et al. (2013) suggests that Hg^{II} enhancements are the result of in-situ oxidation, rather than Hg^{II} from Asian emission sources. However, unlike the study of Timonen et al. (2013), Hg^{II} was anticorrelated to CO in both clusters 1 and 2 of Spring 2022, which seems to argue against an anthropogenic influence.

As an example of this transport regime, data points representing the north Pacific transport regimes in clusters 1 and 2 tend to be concentrated around particular time periods, such as in April 1-3, 2021 (Event 1, Figure 21) where there is a rise in Hg^{II} from 89 pg m^{-3} to 200 pg m^{-3} over 37 hours. During the daytime of April 3, 2021, the air masses measured at SPL appear to suddenly change, shifting to clusters 6 and 7 with lower mean altitudes for the drop and subsequent rise in Hg^{II} values. Interestingly, clusters 6 and 7 have two different directions, the former a westerly mid-altitude flow, and the latter a northerly low-altitude flow. The Hg^{II} peaks during the event occur during the early afternoon and may indicate a diurnal pattern with daytime enhancements (Zwecker, 2021). Because the high Hg^{II} values from clusters 6 and 7 were comparable in magnitude to those from clusters 1 and 2, long-range transport may not be as important as local sources or in situ oxidation chemistry in this case. However, the expected diurnal peak is not existent on April 4, 2021; at that time RH is approximately 30% and likewise water vapor mixing ratio is low at about 3 g/kg. It is therefore unlikely that the low concentrations were due to washout by precipitation. Trace gas measurements were also not much different from the rest of the event, suggesting that there is another factor, perhaps the shift in transport regimes on April 4, 3am, leading to this occurrence of low Hg^{II} on the afternoon of April 4 that is unlike the daytime patterns evident on April 3 or 5.

In contrast to the similarity of the high-altitude transport regimes (clusters 1 and 2 in 2021 and 2022), cluster 7 in Spring 2021 and 2022 that both have a similar northerly continental transport regime are very different in terms of mean Hg^{II} concentration. In Spring 2021, cluster 7 has the highest mean of that season's clusters (103 ± 50 pg m^{-3}), while in Spring 2022 it is the lowest (58 ± 20 pg m^{-3}). The NO_x and O_3 averages in both clusters are similar (Table 1, 2), and their mean cluster heights above ground level are also similar, below 1,000m AGL. However, in terms of relative humidity, the mean value for cluster 7 in Spring 2021 is 60%, and it is 95% in Spring 2022 for the same transport regime. It is therefore possible that the low Hg^{II} levels represented by cluster 7 in Spring 2022 is related to scavenging by clouds and precipitation (Lyman et al., 2020). This is consistent with findings from this project and that of Fäin et al. (2009) that higher Hg^{II} concentrations tend to occur in drier air.

In looking at individual episodes of enhanced Hg^{II}, during the period of April 30 14:00 – May 1 12:00, levels of Hg^{II} drop, corresponding to clusters 5 and 6 at 4pm April 30, 2021 until 12am May 1, 2021 (Event 2, Figure 22). These levels rise again as the day progresses, dropping again just before noon. The Hg^{II} values form a trend during this event that appears almost like a diurnal cycle, with low concentrations at night, but decreases the morning and early afternoon of May 1, 2021 (Fäin et al., 2009). This implies that there are competing sources of Hg^{II}, one with a diurnal behavior and others not.

An interesting occurrence in the Spring 2021 data is cluster 5. From March 13-19, 2021, most of the data points are represented by a low altitude, slower moving transport regime from the west (cluster 5), which has many outliers with Hg^{II} data that are the highest concentrations of the whole study (Figure 8). Noting that RH is temperature dependent, on March 13, 2021 at 2pm, RH was 70%, rising to 94% at 3pm. The highest measurement is 520 pg m^{-3} recorded on March 14, 2021 at 10am, where the relative humidity was 89%. The high RH values continue and decreases to 45% on March 19, 2021. This timeframe coincides with a drop in temperature to around -12º C and rising to above 0ºC at the end of the episode; as such, SPL may have experienced Hg^{II} deposition via snowfall during high humidity and cold temperature. The high Hg^{II} levels recorded during this period could be the result of direct emission or Hg^0 oxidation. If emission, it is unlikely that the Hg^{II} source was local because in that case the data points during this time period would potentially be associated with more clusters than just cluster 5 given that the trajectories used here represent long-range transport, based on relatively course meteorology that is unlikely to capture local differences in transport. Additionally, there is not much difference in water vapor mixing ratio, NO_x, O_3, aerosol scattering PM_{10} in low Hg^{II} values represented by cluster 5. An example is April 19, 8am where Hg^{II} (cluster 5) is 73 pg m^{-3} (2.57 g/kg, 1.9 ppb, 49 ppb, 6.1 Mm^{-1}, respectively), compared with March 15, 2pm where Hg^{II} (cluster 5) is 356 pg m^{-3} (3.14 g/kg, 2.3 ppb, 38 ppb, 2.4 Mm^{-1}, respectively). This suggests that there may be a role of long-range transport associated with this period of notably enhanced Hg^{II}, either transporting Hg^{II} or Hg^0 before oxidation, but additional analysis of these high concentrations March 2021 is ongoing given that the diurnal pattern and extremely high concentrations are not observed to the same degree during other parts of the study.

4.2 Summer Transport Regimes

In Summer 2021, clusters 3 and 4 have the highest Hg^{II} means (125 ± 40 pg m^{-3} and 123 ± 30 pg m^{-3}, respectively). They depict a transport regime from the north Pacific and a northern trans-Pacific transport regime, respectively. While clusters 3 and 4 each represent a high altitude and lower altitude transport pathway, respectively (Figure 14), the two clusters are not statistically different in terms of mean Hg^{II} concentration. In both clusters Hg^{II} is anticorrelated to WV mixing ratio, while Hg^{II} in Cluster 4 is also positively correlated to O_3. Although these transport regimes are similar to the high-altitude transport regimes in Spring 2021 with high Hg^{II} concentrations, Hg^{II} was highest in transport regimes in Spring that had lower Hg^{II} in summer.

In contrast, the lowest mean Hg^{II} is in cluster 6, which represents a southeast transport regime from the direction of the Gulf of Mexico. In this cluster, Hg^{II} is positively correlated to O_3 and SO_2 and has the highest WV mixing ratio mean. Compared to cluster 6, summer cluster 4 (trans-Pacific transport regime) has the lowest WV mixing ratio. This phenomenon is the same in Spring 2021, where the clusters with highest Hg^{II} means also had an anticorrelation between Hg^{II} and WV mixing ratio, supporting again that higher Hg^{II} occurs in drier air (Fäin et al., 2009). The behavior of these two clusters from the two seasons (cluster 4 of Spring 2021 and cluster 6 of Summer 2021 – they both have the lowest Hg^{II} mean of their season) indicate that a positive correlation between Hg^{II} and O_3 does not necessarily also correspond to high average Hg^{II}.

June 8 01:00- June 10 20:00 is the episode (Event 3, Figure 23) in Summer 2021 with the highest Hg^{II} values. The majority of recorded trajectories during this timeframe are from cluster 5, which in summer 2021 is a slow but mid-latitude continental transport regime from the southwest (Figure 14). There are spikes in NO_x, O_3, and aerosol scattering data on June 8 at around 12:00.

This episode is flagged as smoky from biomass burning (Gratz, 2022). Notably, summer Hg^{II} values were higher than both Spring seasons; however, it is important to acknowledge that data corresponding to biomass burning events were not filtered out. This would mean a difference in the air mass composition between the Spring and Summer seasons; the impact of biomass burning on Hg at SPL is an ongoing area of study (Gratz, 2022). Nevertheless, both seasons indicate several comparable transport regimes: a high-altitude, trans-Pacific transport regime, westerly transport regimes below 4000m AGL, and a northerly continental low-altitude transport regime. A summary figure (Figure 20) shows a boxplot of Hg^{II} concentrations of the three notable transport regimes: trans-Pacific, low-altitude central Pacific, and northerly continental. There was, however, not a southeast cluster generated for the Spring seasons by HYSPLIT.

In addition, although westerly transport regimes, which generally have higher transport altitudes, do show elevated Hg^{II}, high Hg^{II} values do not necessarily seem to be strongly dependent on trajectory altitude. For example, in Spring 2021, the highest Hg^{II} mean is found in the transport regime with the lowest average altitude of the clusters. In contrast, in Spring 2022 the highest Hg^{II} mean is in a high-altitude trans-Pacific transport regime. In Summer 2021, the highest Hg^{II} means are found in clusters 3 and 4, and although their Hg^{II} means are similar, there is much difference in the average altitude of their transport regimes. The summer northerly continental transport regime with the lowest average altitude does not have the lowest Hg^{II} means (117 ± 20 pg m^{-3}); the cluster with the lowest Hg^{II} mean is cluster 6 from the direction of the Gulf, which has similar altitude to that of cluster 3 (cluster with highest Hg^{II} mean). These comparisons indicate that air mass height above ground level may not be the most important predictor of Hg^{II} concentration on average, and therefore air mass composition and the potential for Hg^0 oxidation may be more important, particularly in drier air masses.

4.3 Fall Transport Regimes

Note that Fall 2021 has only 40 days of data, compared to the three-months measurement periods of Spring and Summer. During the measurement period, cluster 4 which represents a higher-altitude trans-Pacific transport has the highest Hg^{II} means (138 ± 40 pg m^{-3}). Hg^{II} in this transport regime is positively correlated to O_3, SO_2, PM_{10} and PM_1 aerosol scattering, and anticorrelated to WV mixing ratio. Other clusters with higher Hg^{II} values are influenced by prevailing westerlies, while the transport regimes (clusters 1 and 2) that represent a southwest and southeast transport, respectively have lower Hg^{II} means. This suggests that westerly long-range transport may be a contributor to higher Hg^{II} measurements, a pattern consistent with Spring and Summer 2021. Meanwhile, all transport regimes except the one associated with transport from the Gulf of Mexico show an anticorrelation between Hg^{II} and WV mixing ratio. This again indicates that higher Hg^{II} occurs in drier air.

Cluster 2 in Fall 2021 has a similar transport regime as cluster 6 in Summer 2021, both having a southeast direction from the Gulf. Both have the lowest Hg^{II} mean among the clusters. However, while cluster 6 of Summer 2021 has the highest O_3 mean (60 ± 9 ppb), cluster 2 of Fall 2021 has the lowest O_3 mean (47 ± 7 ppb), suggesting that the Hg^{II} levels may be independent of O_3 concentration (Fäin et al., 2009).

The clusters generated by HYSPLIT for both Summer and Fall 2021 are similar, both indicating westerly transport regimes and a southeasterly transport regime from the direction of the Gulf of Mexico. However, a low-altitude northerly continental transport regime was not generated for the Fall season, suggesting that this transport regime occurs more in the earlier than latter months of the year. Further HYSPLIT analysis throughout the year and over multiple seasons would be necessary to verify this observation.

5. Conclusions

In this study, we used chemical and meteorological measurements at SPL to expand on past work examining air mass characterization of larger-scale transport relating to Hg oxidation. Using HYSPLIT cluster analysis and the study of episodic events, we found that enhanced Hg^{II} concentrations occurred in drier air masses consistently throughout the measurement period, with both long-range transport and in-situ chemistry as likely Hg^{II} drivers. Springtime data show similar meteorological patterns across the two years, and slightly higher Hg^{II} levels in spring 2022. Data from the Summer and early Fall months indicate that southeasterly flow from the Gulf of Mexico was associated with lower Hg^{II} in higher humidity air masses.

These results inform ongoing analysis of the chemistry of Hg measured at continental high elevation sites like SPL. Areas of future research include identifying the location of Hg oxidation along the back-trajectory, to understand whether the oxidation happened some distance upwind or in the air around SPL, and re-running the cluster analysis without smoke periods to look at summertime transport regimes in non-smoke impacted air masses. More research should also be conducted on a case study of cluster 5 of spring 2021 from March 13-19, 2021, where extremely high Hg^{II} values occurred. Modeling transport regimes in mountainous terrain is difficult, and further studies can experiment with different starting heights AGL at SPL to see if different conclusions are reached and different air mass transport regimes are resolved. Repeating the cluster analysis with higher resolution meteorology than GDAS could be worthwhile, since the GDAS gridded meteorology is quite coarse. We anticipate our work to add to the understanding of transport regimes of atmospheric Hg to inform scientific understanding of mercury origins and chemistry.

Figures

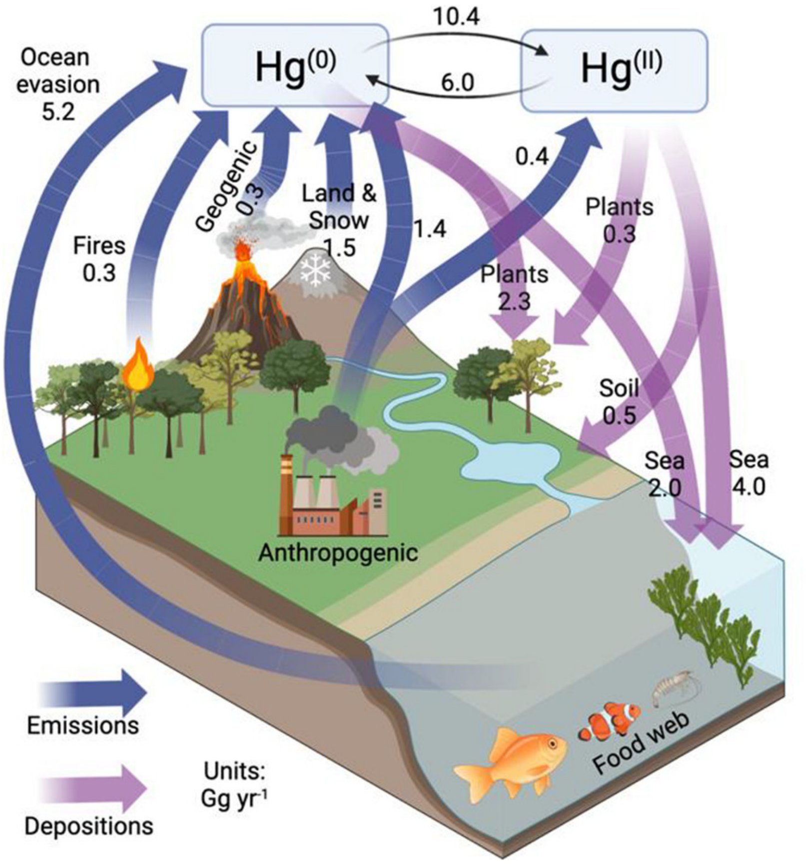

Figure 1. Mercury cycle and estimates of fluxes (Gg yr^{-1}). Figure courtesy of Castro et al. (2022).

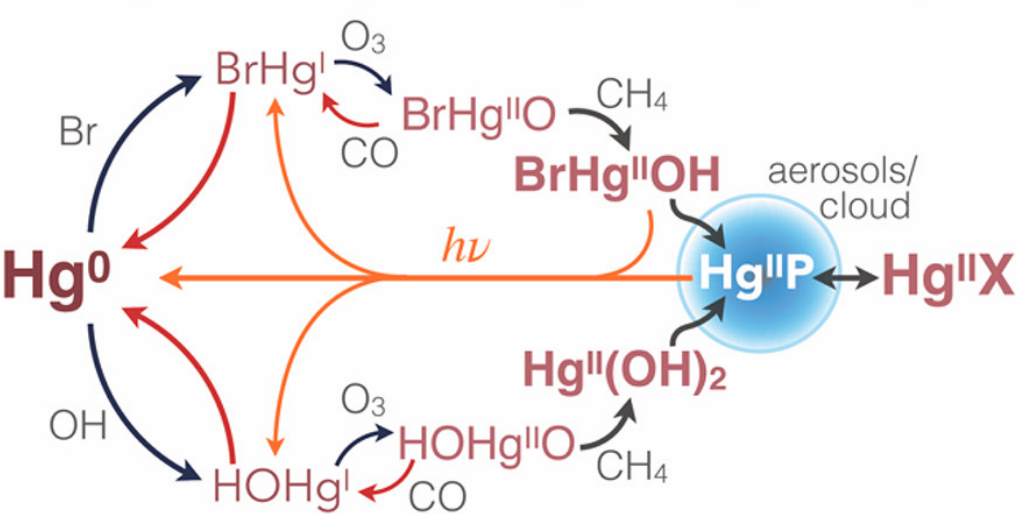

Figure 2. Major atmospheric mercury redox pathways. Figure courtesy of Shah et al. (2021).

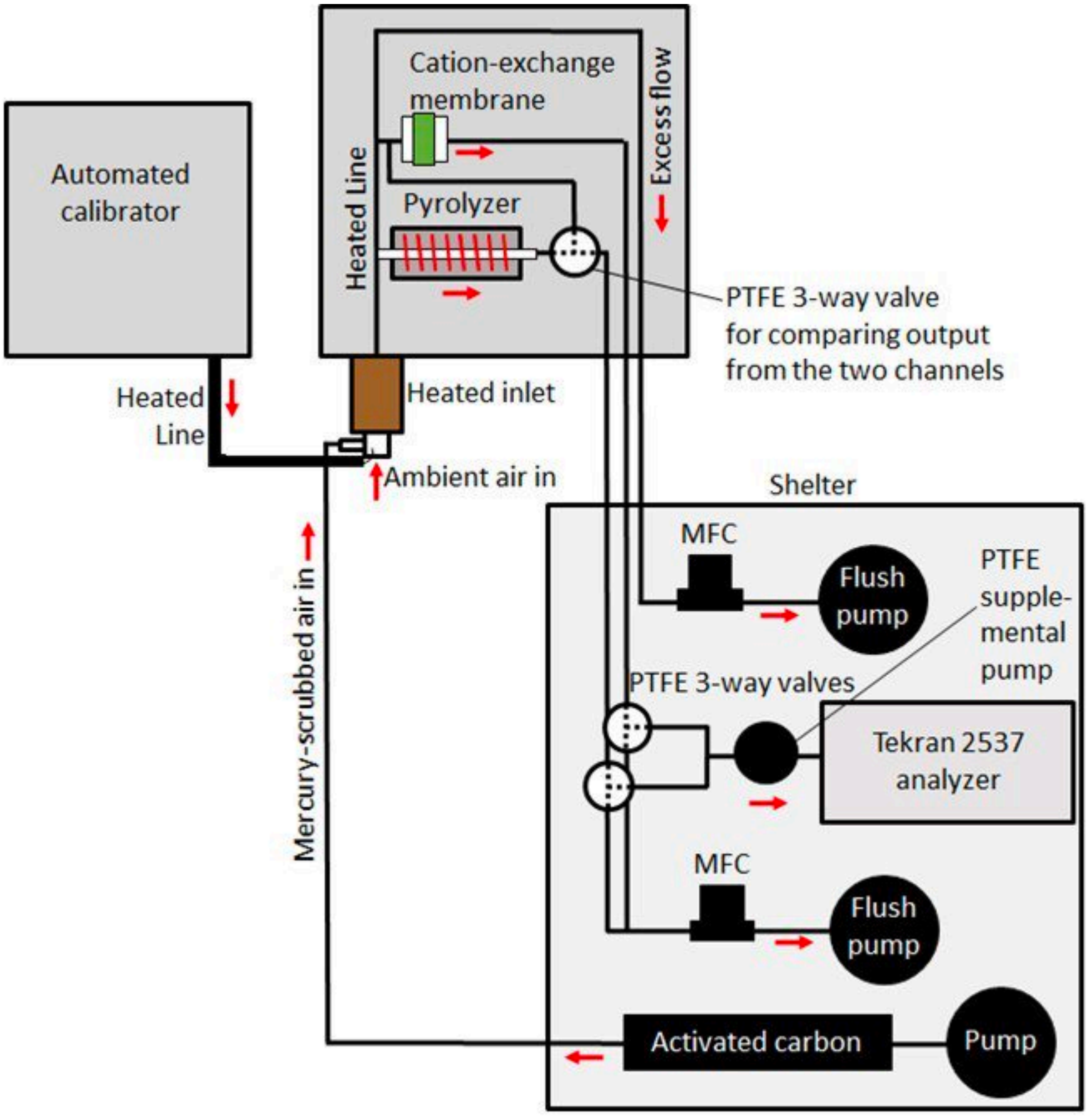

Figure 3. Diagram of the Utah State University dual-channel mercury measurement system and calibrator. Figure courtesy of Dr. Seth Lyman.

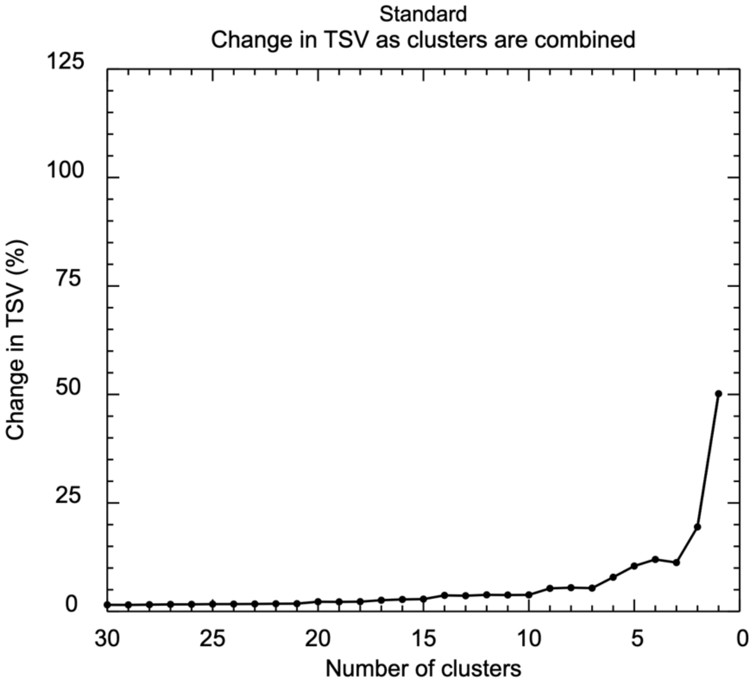

Figure 4. HYSPLIT Total Spatial Variance Plot for the Spring 2021 Cluster Analysis.

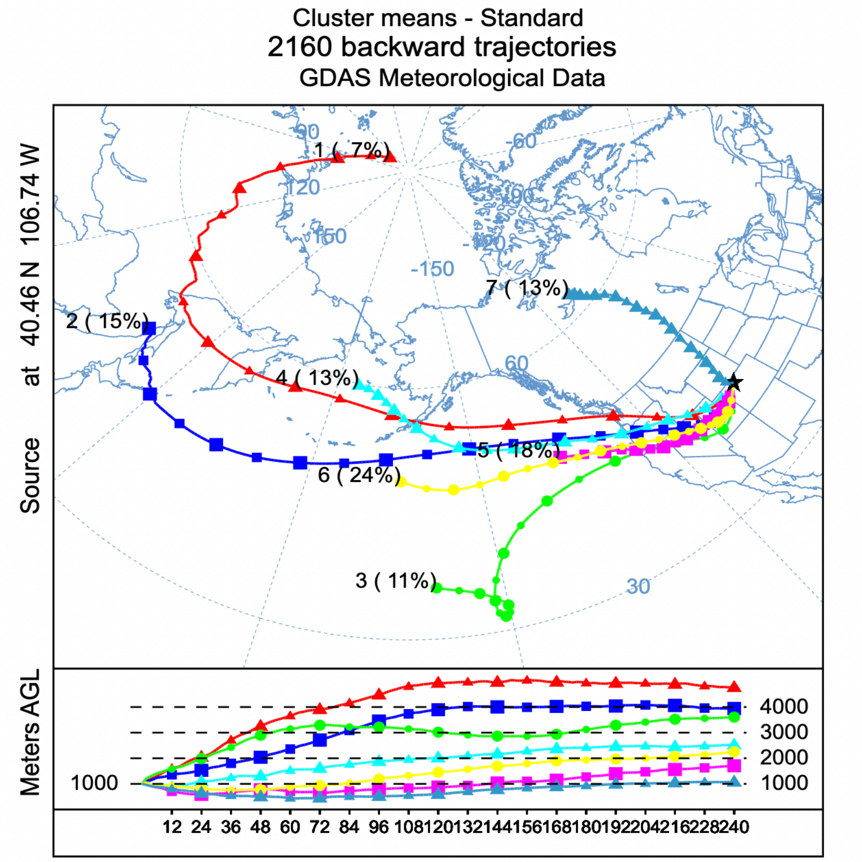

Figure 5. HYSPLIT Cluster Analysis Means Plot for Spring 2021 (March 12 – May 31, 2021).

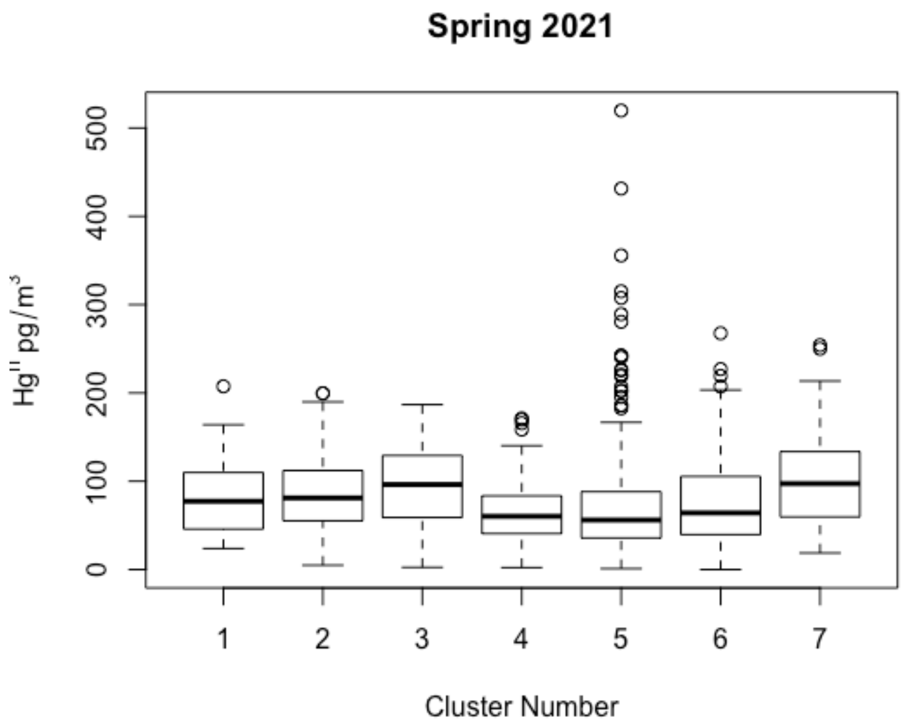

Figure 6. Boxplot of Hg^{II} concentrations within each cluster for Spring 2021 (March 12 – May 31, 2021).

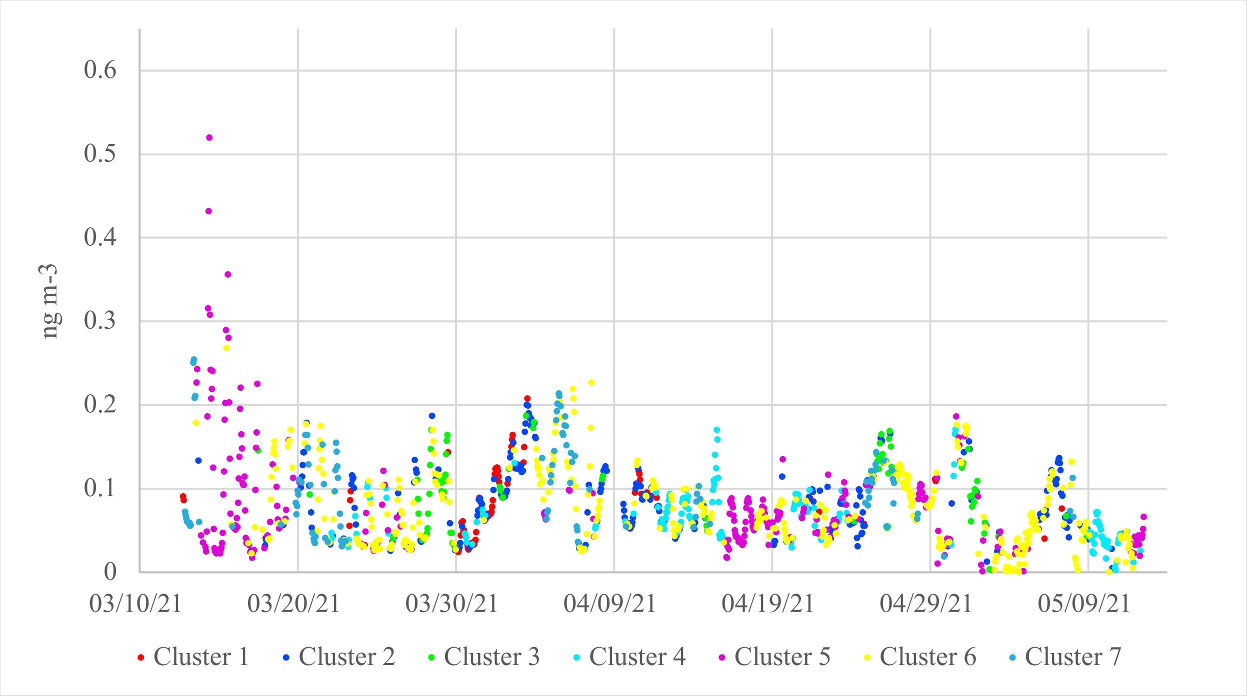

Figure 7. Hourly-averaged Hg^{II} concentrations in Spring 2021, differentiated by color for the corresponding cluster number. The merging is based on the timestamp of the hourly measurement and the start time of the hourly trajectory, which is the same for the other seasons.

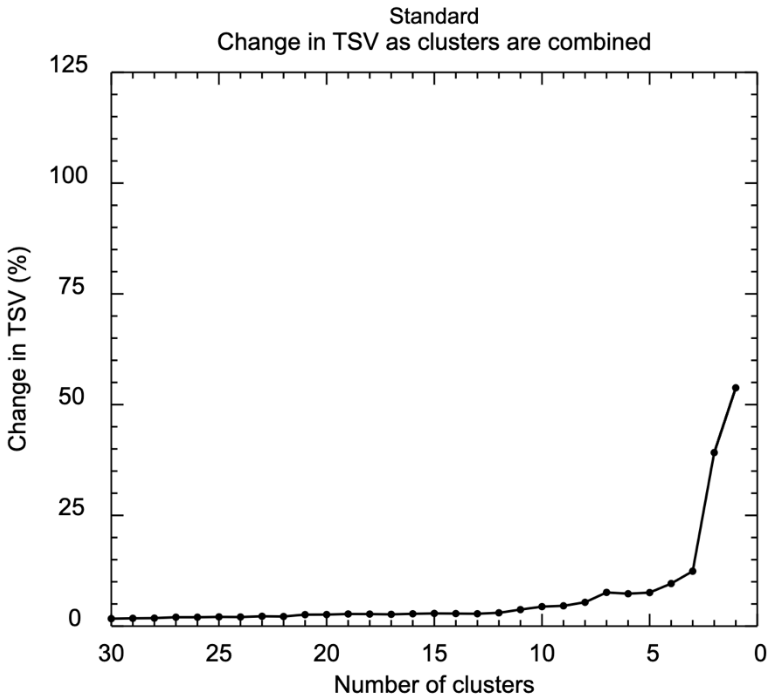

Figure 8. HYSPLIT Total Spatial Variance Plot for the Spring 2022 Cluster Analysis.

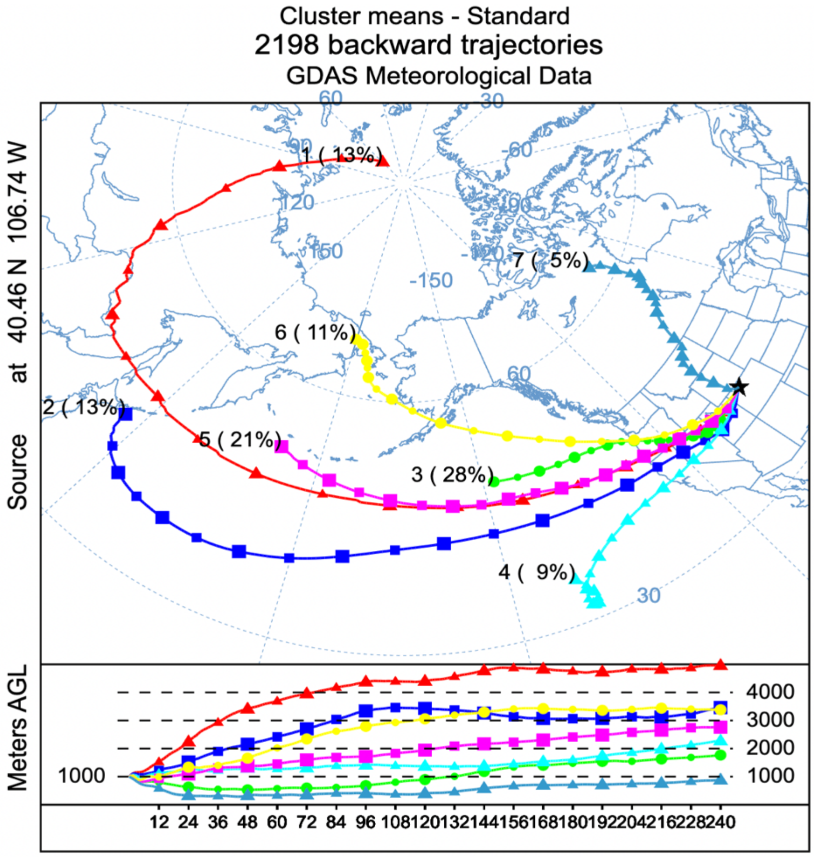

Figure 9. HYSPLIT Cluster Analysis Means Plot for Spring 2022 (March 1 – May 31, 2022).

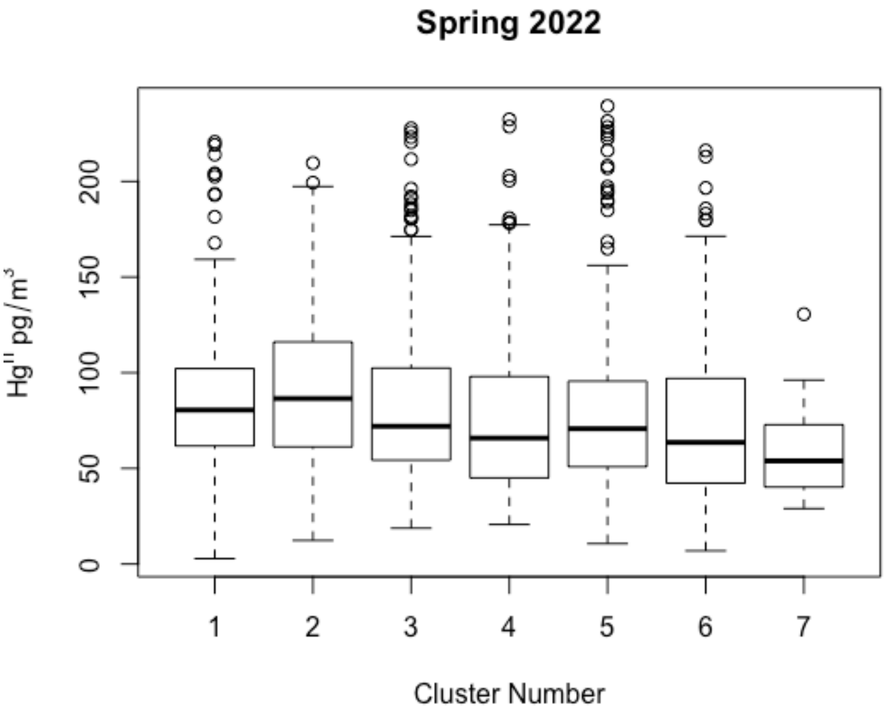

Figure 10. Boxplot of Hg^{II} concentrations within each cluster for Spring 2022 (March 1 – May 31, 2022).

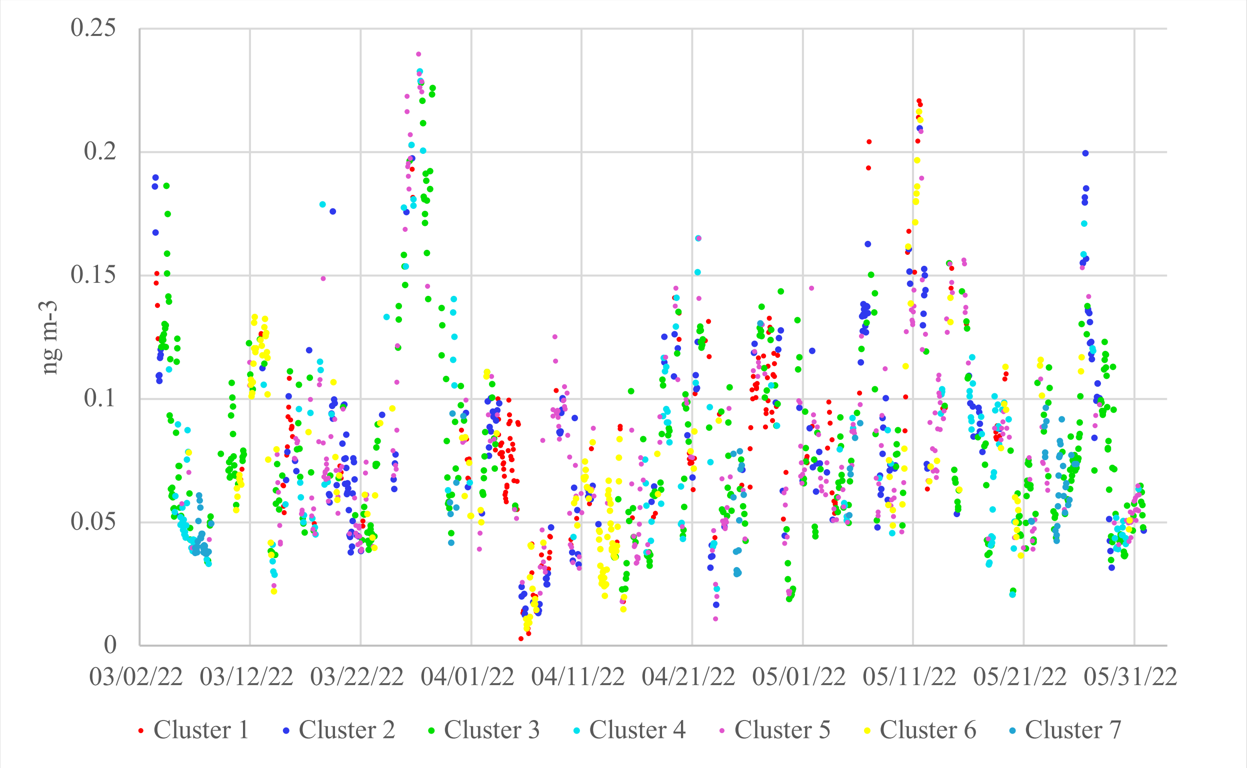

Figure 11. Hg^{II} concentration in Spring 2022, differentiated by color for cluster number.

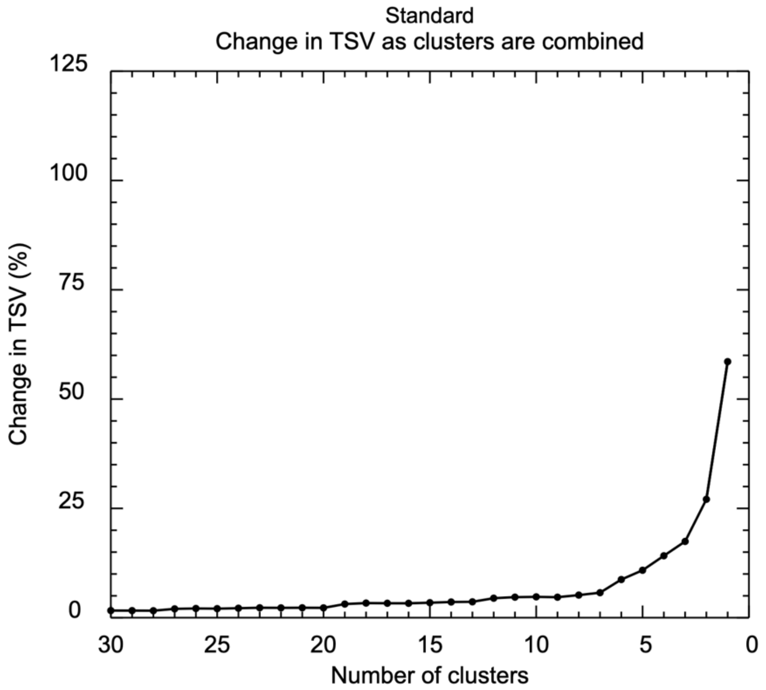

Figure 12. HYSPLIT Total Spatial Variance Plot for the Summer 2021 Cluster Analysis.

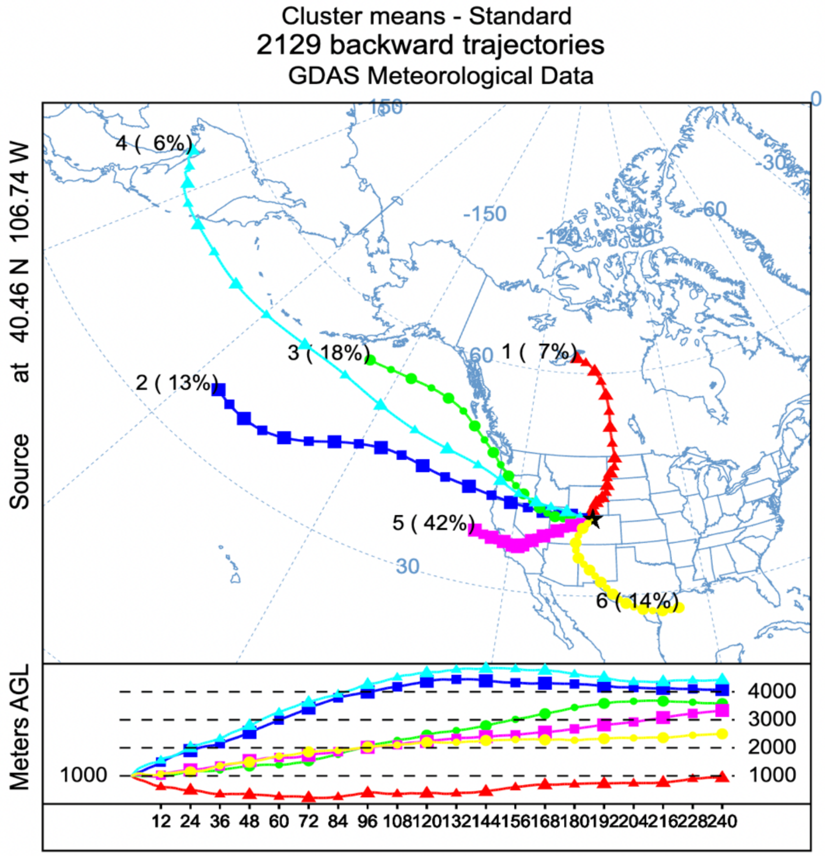

Figure 13. HYSPLIT Cluster Analysis Means Plot for Summer 2021 (June 1 – August 31, 2021).

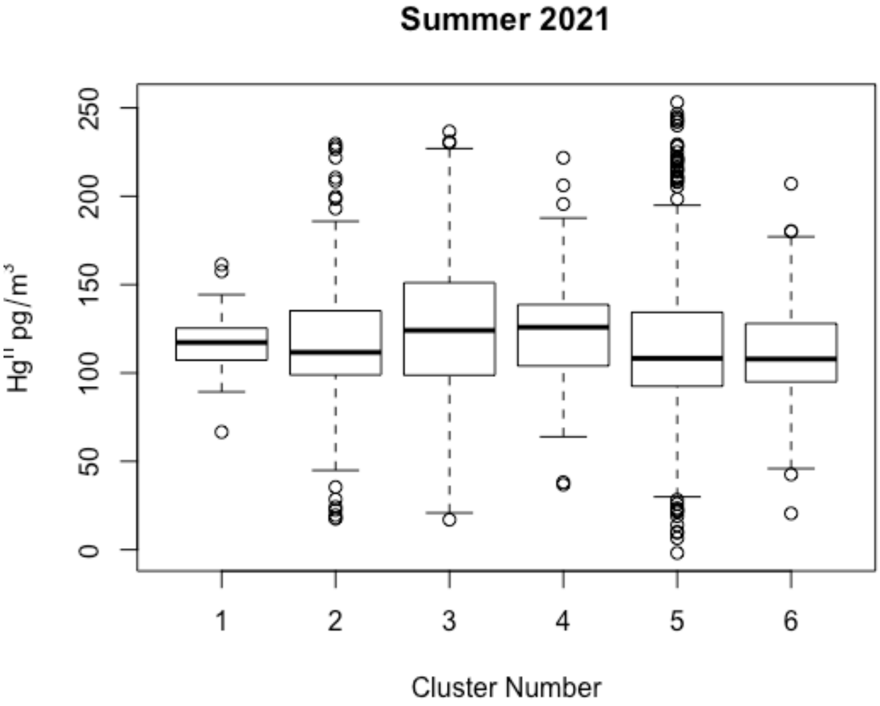

Figure 14. Boxplot of Hg^{II} concentrations within each cluster for Summer 2021 (June 1 – August 31, 2021).

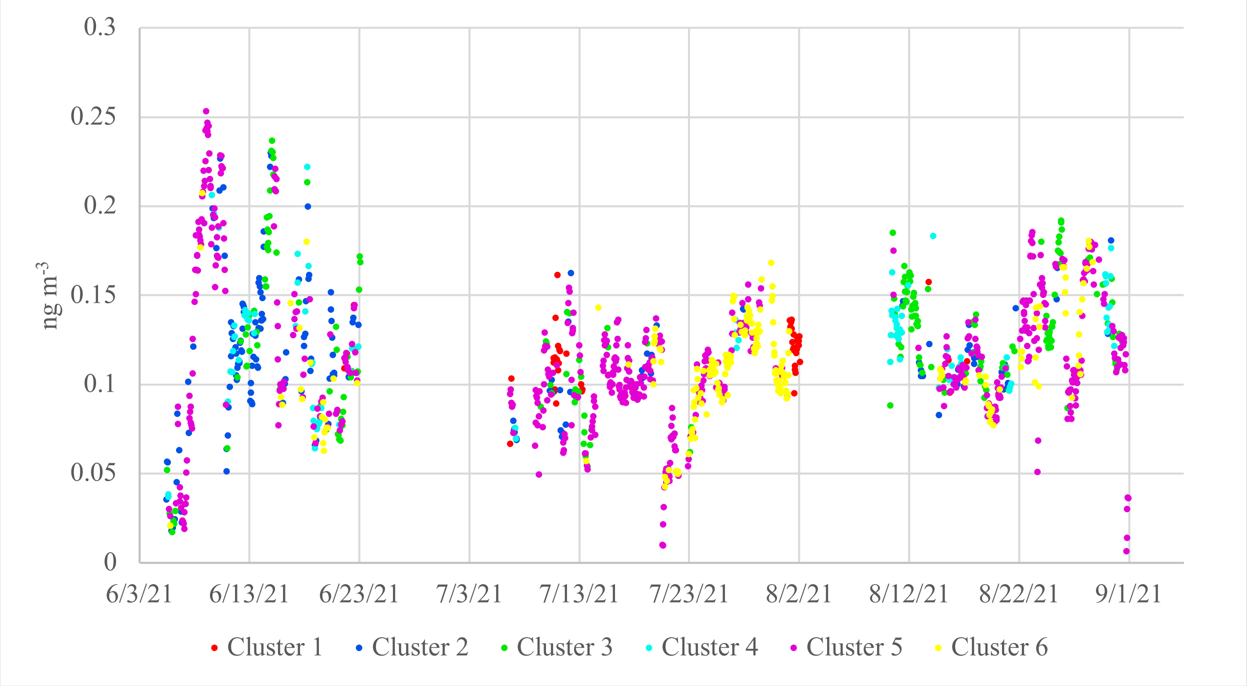

Figure 15. Hg^{II} concentration in Summer 2021, differentiated by color for cluster number.

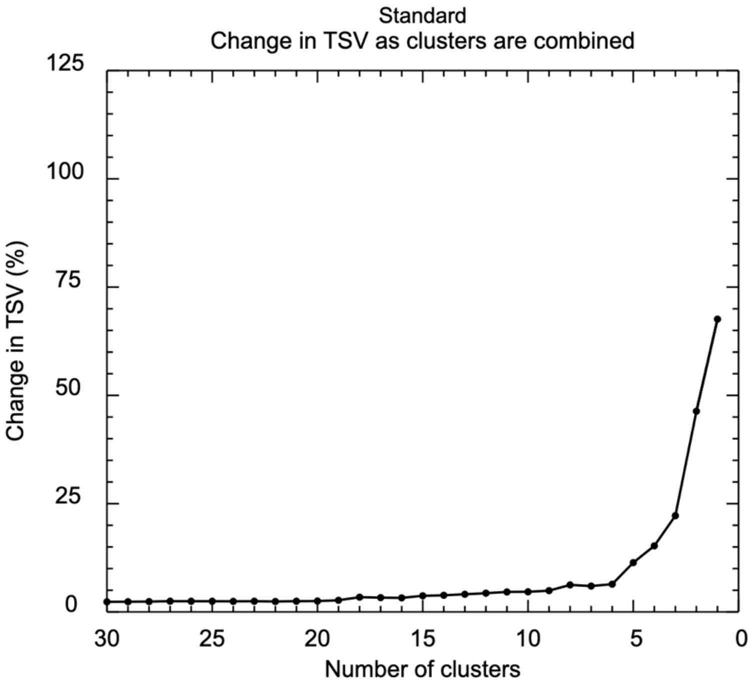

Figure 16. HYSPLIT Total Spatial Variance Plot for the Fall 2021 Cluster Analysis.

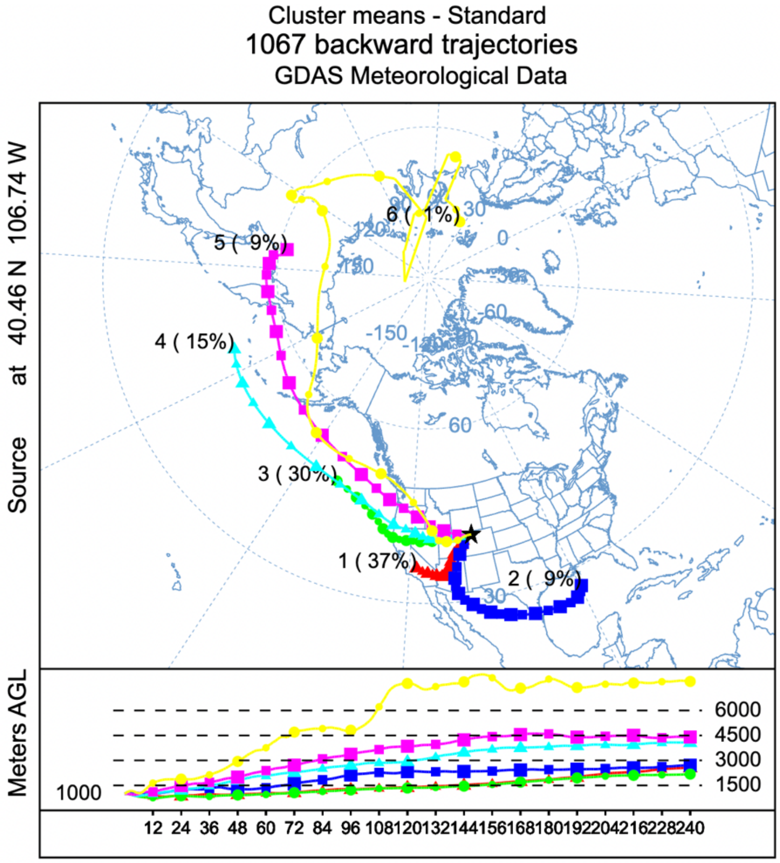

Figure 17. HYSPLIT Cluster Analysis Means Plot for Fall 2021 (September 1 – October 10, 2021).

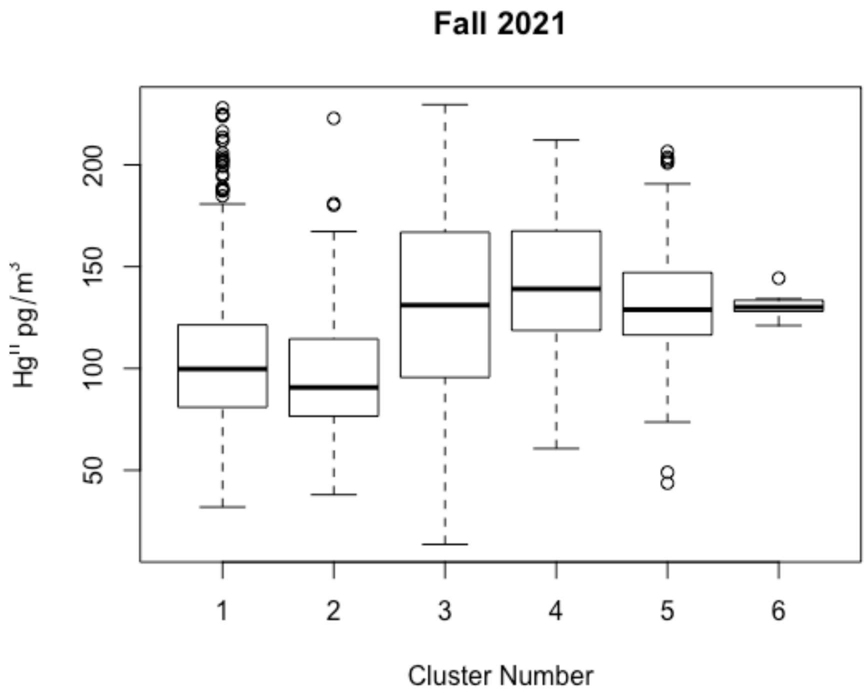

Figure 18. Boxplot of Hg^{II} concentrations within each cluster for Fall 2021 (September 1 – October 10, 2021).

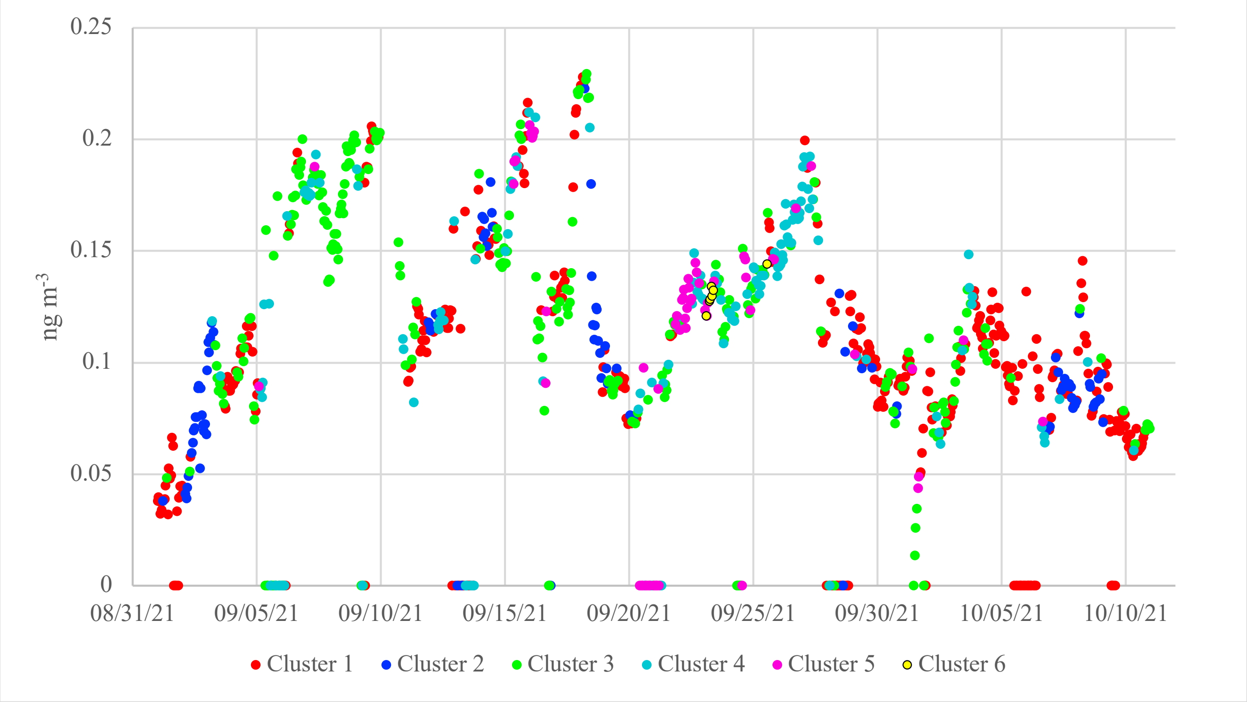

Figure 19. Hg^{II} concentration in Fall 2021, differentiated by color for cluster number.

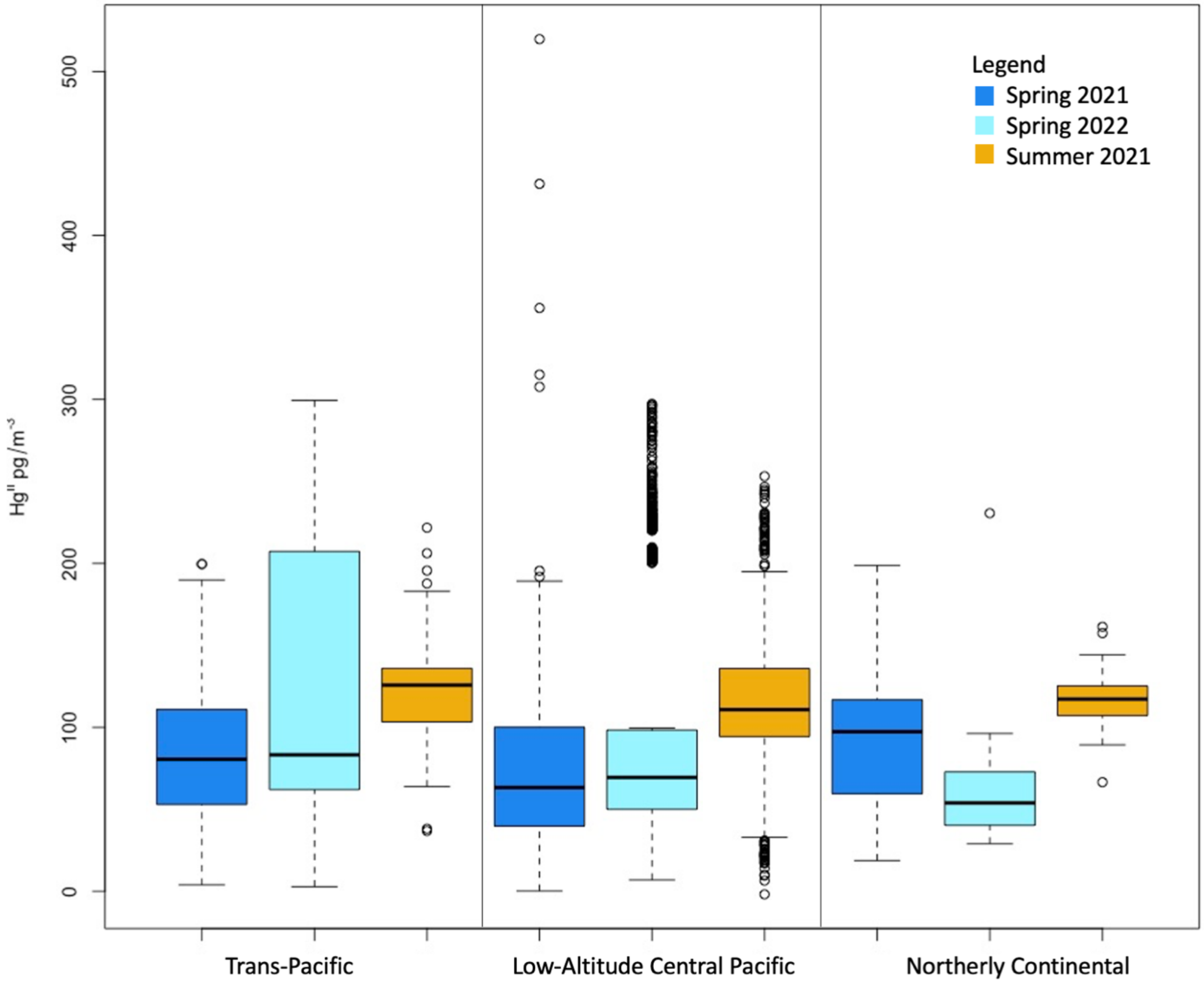

Figure 20. Boxplot of Hg^{II} concentrations of the three notable transport regimes. Clusters within a given season have been grouped based on common directional origins for ease of comparison. The trans-pacific transport regime of Spring 2021 consists of clusters 1 and 2, of Spring 2022 clusters 1 and 2, and of Summer 2021 cluster 4. The low-altitude central pacific transport regime of Spring 2021 consists of clusters 3, 4, 5, and 6, of Spring 2022 clusters 3, 4, 5, and 6, and of Summer 2021 cluster 2, 3, and 5. The northerly continental transport regime of Spring 2021 consists of cluster 7, of Spring 2022 cluster 7, and of Summer 2021 cluster 1.

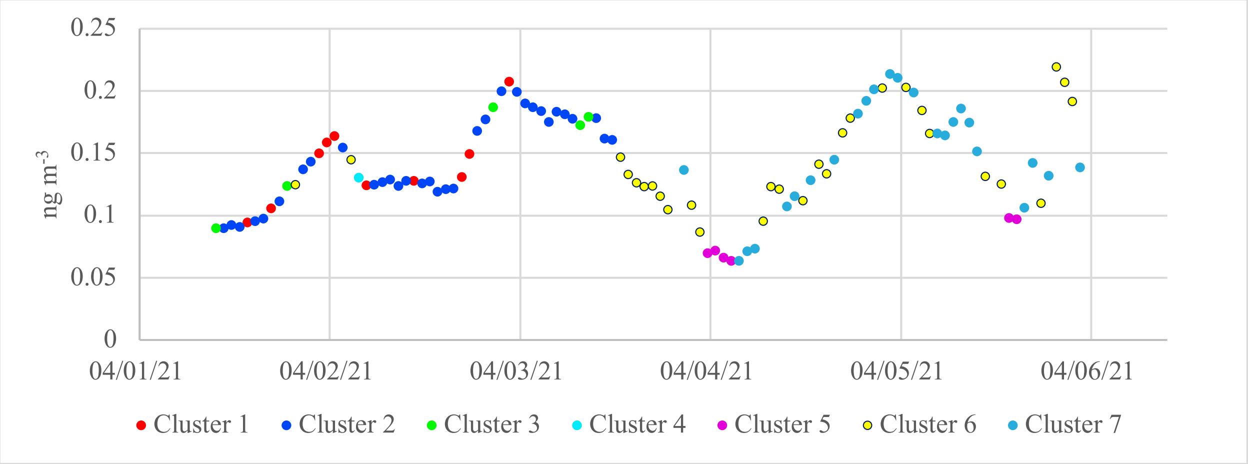

Figure 21. Hg^{II} concentration in Event 1: April 2 00:00 – April 6 13:00.

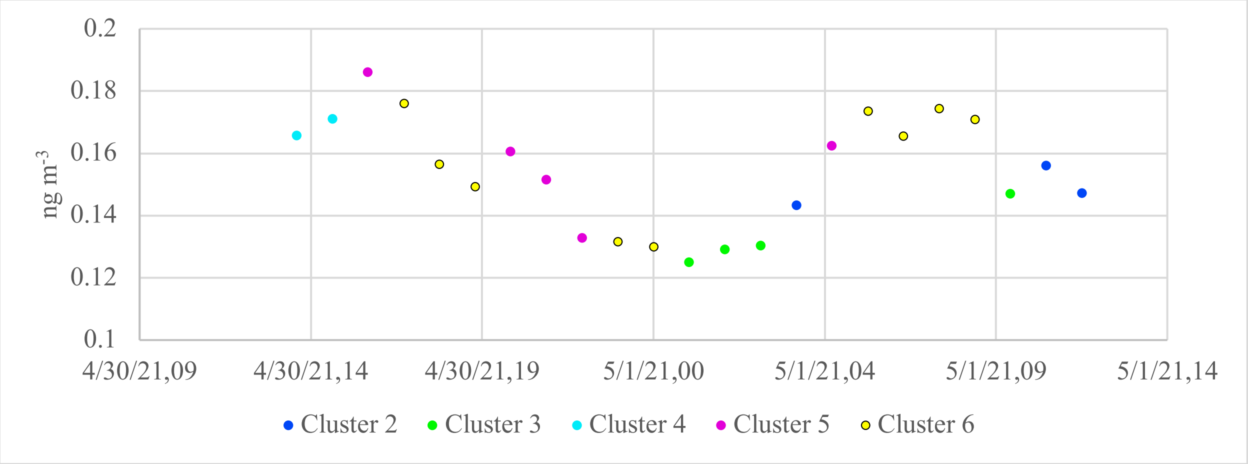

Figure 22. Hg^{II} concentration in Event 2: April 30 14:00 – May 1 12:00.

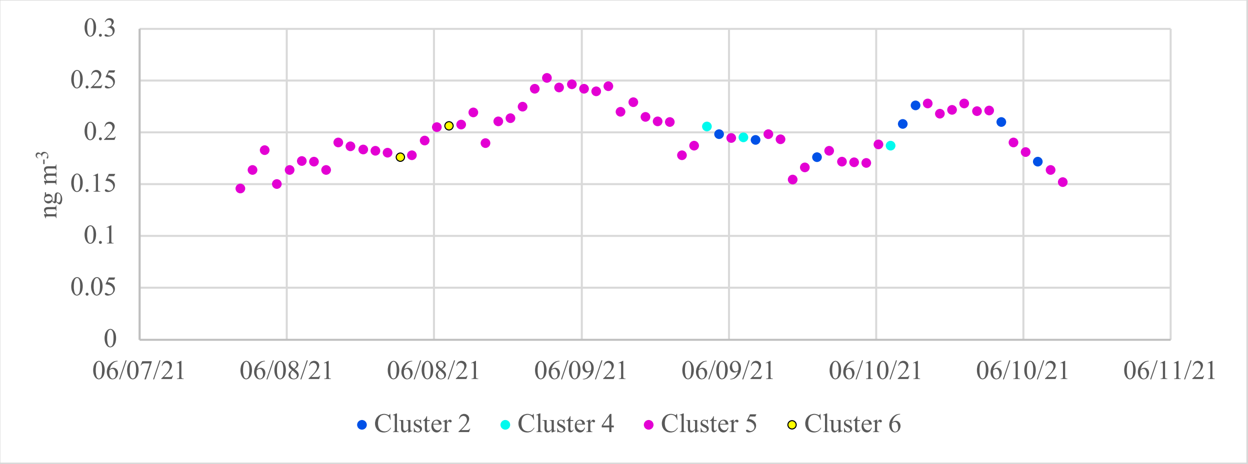

Figure 23. Hg^{II} concentration in Event 3: June 8 01:00 – June 10 20:00.

Tables

Table 1. Summary of hourly-averaged data from March 12 – May 31, 2021														
	Mean	SD	Mean	SD	Mean	SD	Mean	SD	Mean	SD	Mean	SD	Mean	SD
	Cluster 1		Cluster 2		Cluster 3		Cluster 4		Cluster 5		Cluster 6		Cluster 7	
Hg^0 (ng m^{-3})	1.3	± 0.2	1.3	± 0.1	1.3	± 0.1	1.3	± 0.1	1.3	± 0.1	1.3	± 0.1	1.3	± 0.1
Hg^{II} (pg m^{-3})	80	± 40	85	± 40	93	± 40	61	± 50	75	± 70	69	± 60	103	± 50
O_3 (ppb)	45	± 7	49	± 7	49	± 9	51	± 9	46	± 9	49	± 9	49	± 7
NO_x (ppb)	1.9	± 0.2	1.9	± 0.2	1.9	± 0.2	2.0	± 0.2	1.9	± 0.2	1.9	± 0.2	1.9	± 0.3
PM_1 scattering (Mm-1)	3.7	± 2.6	3.4	± 1.4	3.2	± 1.6	2.9	± 1.5	2.8	± 1.5	2.8	± 1.7	4.0	± 2.0
WV Mixing Ratio (g/kg)	1.8	± 0.7	2.6	± 1.0	3.1	± 0	2.6	± 0.9	3.1	± 1.0	3.1	± 1.0	3.5	± 1.3

Note: Cells highlighted in red signify the highest mean among the clusters, and blue signify the lowest mean. Light red is used to highlight the second highest mean with concentrations close to the highest. Measurements are not highlighted when the means are the same or similar. The above statements are applicable to Tables 1-4.

Table 2. Summary of hourly-averaged data from March 1 – May 31, 2022														
	Mean	SD	Mean	SD	Mean	SD	Mean	SD	Mean	SD	Mean	SD	Mean	SD
	Cluster 1		Cluster 2		Cluster 3		Cluster 4		Cluster 5		Cluster 6		Cluster 7	
Hg^0 (ng m^{-3})	1.3	± 0.1	1.2	± 0.1	1.3	± 0.1	1.3	± 0.1	1.3	± 0.1	1.3	± 0.1	1.3	± 0.1
Hg^{II} (pg m^{-3})	85	± 40	88	± 40	81	± 40	78	± 40	80	± 40	72	± 40	58	± 20
CO (ppb)	134	± 21	126	± 20	134	± 20	127	± 18	135	± 19	141	± 20	140	± 17
NO_x (ppb)	1.2	± 0.9	1.1	± 0.9	1.3	± 1.2	1.2	± 0.9	1.3	± 0.8	1.3	± 0.9	1.8	± 1.7
O_3 (ppb)	53	± 7	51	± 6	51	± 6	51	± 6	51	± 6	51	± 5	50	± 5
PM_1 scattering (Mm-1)	2.4	± 2.4	2.4	± 2.0	2.4	± 0	1.9	± 1.5	2.2	± 1.6	1.6	± 1.0	2.7	± 1.4
WV Mixing Ratio (g/kg)	2.7	± 2.7	3.0	± 1.0	3.1	± 1.0	3.3	± 1.1	3.1	± 1.0	2.5	± 0.8	3.0	± 1.2

Note: The Hg^0 mean for cluster 6 is rounded from 1.2803, which is higher than that of other clusters.

Table 3. Summary of hourly-averaged data from June 1 – August 31, 2021												
	Mean	SD	Mean	SD	Mean	SD	Mean	SD	Mean	SD	Mean	SD
	Cluster 1		Cluster 2		Cluster 3		Cluster 4		Cluster 5		Cluster 6	
Hg^0 (ng m^{-3})	1.3	± 0.1	1.2	± 0.2	1.2	± 0.1	1.2	± 0.1	1.2	± 0.2	1.3	± 0.1
Hg^{II} (pg m^{-3})	117	± 20	116	± 40	125	± 40	123	± 30	115	± 40	110	± 30
CO (ppb)	189	± 78	232	± 211	219	± 92	244	± 84	201	± 98	171	± 55
NO_x (ppb)	2.0	± 0.3	2.0	± 0.3	2.0	± 0.4	2.0	± 0.2	2.1	± 0.4	2.1	± 0.3
O_3 (ppb)	56	± 7	54	± 8	56	± 8	56	± 7	58	± 8	60	± 9
PM_1 scattering (Mm-1)	19.4	± 38.6	23.1	± 41.0	30.7	± 47.8	33.8	± 39.2	36.6	± 52.5	29.8	± 42.8
WV Mixing Ratio (g/kg)	6.1	± 2.1	4.8	±1.8	5.2	± 1.9	4.7	± 1.6	5.8	± 1.9	7.4	± 2.2

Table 4. Summary of hourly-averaged data from September 1 – October 10, 2021												
	Mean	SD	Mean	SD	Mean	SD	Mean	SD	Mean	SD	Mean	SD
	Cluster 1		Cluster 2		Cluster 3		Cluster 4		Cluster 5		Cluster 6	
Hg^0 (ng m^{-3})	1.3	± 0.1	1.3	± 0.1	1.2	± 0.1	1.2	± 0.1	1.2	± 0.1	1.1	± 0
Hg^{II} (pg m^{-3})	106	± 40	99	± 30	133	± 40	138	± 40	135	± 40	131	± 10
CO (ppb)	157	± 28	167	± 42	192	± 48	173	± 43	166	± 33	153	± 18
NO_x (ppb)	2.4	± 1.3	2.3	± 1.0	2.4	± 1.2	2.1	± 1.3	1.9	± 0.7	1.9	± 0.3
O_3 (ppb)	49	± 8	47	± 7	56	± 9	55	± 8	54	± 9	51	± 2
PM_1 scattering (Mm-1)	10.4	± 10.7	42.2	± 16.4	25.8	± 23.1	16.0	± 18.9	8.8	± 15.0	7.2	± 6.2
WV Mixing Ratio (g/kg)	5.3	± 1.7	6.5	± 1.7	3.9	± 1.6	3.6	± 1.4	3.3	± 1.2	2.9	± 0.5

Note: The Hg^0 mean for cluster 1 is rounded from 1.2539, and cluster 2 from 1.2549.

Table 5. Pearson correlation coefficients in Spring 2021 of Hg^{II} to the below measurements.

P-value significance indicated by **<0.01; *<0.05

		Hg^0	NOx	O$_3$	SO$_2$	PM$_{10}$ scattering	PM$_1$ scattering	WV mixing ratio (g/kg)
Pearson Correlation	1	-.623**	-0.191	0.184	-0.199	.529**	.453**	0.136
Sig. (2-tailed)		0.000	0.098	0.111	0.084	0.000	0.000	0.242
N		76	76	76	76	76	76	76
Pearson Correlation	2	-.659**	-0.017	-0.101	.130*	.229**	.168**	-.244**
Sig. (2-tailed)		0.000	0.793	0.111	0.040	0.000	0.008	0.000
N		249	245	249	249	249	249	249
Pearson Correlation	3	-.730**	-0.192	0.013	.212*	-0.157	-0.167	-.440**
Sig. (2-tailed)		0.000	0.071	0.900	0.044	0.138	0.114	0.000
N		91	89	91	91	91	91	91
Pearson Correlation	4	-.330**	0.084	.270**	.173*	.302**	.296**	-0.099
Sig. (2-tailed)		0.000	0.284	0.000	0.026	0.000	0.000	0.206
N		166	166	166	166	166	166	166
Pearson Correlation	5	-.136*	0.095	-0.082	0.013	-0.094	-0.057	0.050
Sig. (2-tailed)		0.025	0.117	0.174	0.827	0.121	0.352	0.407
N		273	273	273	273	272	273	273
Pearson Correlation	6	-.497**	0.011	0.051	0.083	.312**	.315**	-.340**
Sig. (2-tailed)		0.000	0.829	0.304	0.090	0.000	0.000	0.000
N		415	415	415	415	415	415	415
Pearson Correlation	7	-.500**	-0.182	-0.011	-0.091	0.188	0.122	-.358**
Sig. (2-tailed)		0.000	0.059	0.912	0.346	0.051	0.206	0.000
N		109	109	109	109	109	109	109

Table 6. Pearson correlation coefficients in Spring 2022 of Hg^{II} to the below measurements.
P-value significance indicated by $^{**}<0.01$; $^{*}<0.05$

		Hg^0	CO	NOx	O_3	SO_2	PM_{10} scattering	PM_1 scattering	WV mixing ratio (g/kg)
Pearson Correlation	1	-.624**	-.228**	-0.105	.293**	0.018	.236**	.238**	.253**
Sig. (2-tailed)		0.000	0.001	0.131	0.000	0.798	0.001	0.001	0.000
N		209	209	208	209	207	209	209	209
Pearson Correlation	2	-.579**	-.322**	-0.109	.211**	0.061	.239**	.226**	.150*
Sig. (2-tailed)		0.000	0.000	0.097	0.001	0.355	0.000	0.001	0.022
N		233	233	233	233	233	233	233	233
Pearson Correlation	3	-.612**	-.255**	-0.039	.145**	.181**	.325**	.259**	-.172**
Sig. (2-tailed)		0.000	0.000	0.401	0.002	0.000	0.000	0.000	0.000
N		459	459	459	459	456	459	459	459
Pearson Correlation	4	-.530**	-.240**	-0.115	0.040	.331**	.370**	.303**	-0.124
Sig. (2-tailed)		0.000	0.002	0.144	0.615	0.000	0.000	0.000	0.113
N		164	164	164	164	164	164	164	164
Pearson Correlation	5	-.643**	-.364**	-0.088	0.044	.204**	.261**	.170**	-0.019
Sig. (2-tailed)		0.000	0.000	0.094	0.404	0.000	0.000	0.001	0.715
N		360	360	360	360	360	360	360	360
Pearson Correlation	6	-.516**	-.327**	-.222**	.238**	.182*	0.072	.176*	.375**
Sig. (2-tailed)		0.000	0.000	0.003	0.001	0.016	0.341	0.018	0.000
N		179	179	179	179	175	179	179	179
Pearson Correlation	7	.226*	0.213	-0.104	.397**	-0.199	.340**	0.112	.588**
Sig. (2-tailed)		0.040	0.053	0.351	0.000	0.072	0.002	0.312	0.000
N		83	83	83	83	83	83	83	83

Table 7. Pearson correlation coefficients in Summer 2021 of Hg^{II} to the below measurements.
P-value significance indicated by **<0.01; *<0.05

		Hg^0	CO	NOx	O_3	SO_2	PM_{10} scattering	PM_1 scattering	WV mixing ratio (g/kg)
Pearson Correlation	1	$-.319^{*}$	0.223	0.268	-0.036	0.263	0.209	0.230	0.071
Sig. (2-tailed)		0.021	0.132	0.055	0.800	0.060	0.137	0.100	0.619
N		52	47	52	52	52	52	52	52
Pearson Correlation	2	$-.588^{**}$	0.008	-0.083	-0.099	0.097	-0.023	-0.020	$-.449^{**}$
Sig. (2-tailed)		0.000	0.948	0.323	0.237	0.187	0.757	0.792	0.000
N		185	65	143	143	185	185	184	185
Pearson Correlation	3	$-.780^{**}$	-0.153	$-.244^{**}$	-0.057	0.002	-0.046	-0.070	$-.628^{**}$
Sig. (2-tailed)		0.000	0.066	0.001	0.427	0.982	0.505	0.314	0.000
N		209	144	200	200	209	209	209	209
Pearson Correlation	4	$-.525^{**}$	0.162	0.074	$.457^{**}$	0.164	0.184	0.180	$-.494^{**}$
Sig. (2-tailed)		0.000	0.233	0.511	0.000	0.108	0.070	0.075	0.000
N		98	56	82	82	98	98	98	98
Pearson Correlation	5	$-.771^{**}$	$.110^{*}$	$-.195^{**}$	-0.041	0.019	-0.017	-0.027	$-.585^{**}$
Sig. (2-tailed)		0.000	0.023	0.000	0.332	0.662	0.686	0.525	0.000
N		578	427	552	552	551	576	576	577
Pearson Correlation	6	$-.564^{**}$	0.050	-0.070	$.153^{*}$	$.206^{**}$	0.093	0.088	$-.338^{**}$
Sig. (2-tailed)		0.000	0.491	0.312	0.025	0.003	0.176	0.200	0.000
N		214	191	214	214	213	213	213	214

Table 8. Pearson correlation coefficients in Fall 2021 of Hg^{II} to the below measurements.
P-value significance indicated by **<0.01; *<0.05

		Hg^0	CO	NOx	O_3	SO_2	PM_{10} scattering	PM_1 scattering	WV mixing ratio (g/kg)
Pearson Correlation	1	-.570**	-0.006	-.156**	.577**	0.053	.191**	.174**	-.597**
Sig. (2-tailed)		0.000	0.919	0.005	0.000	0.337	0.001	0.002	0.000
N		327	257	327	327	327	325	325	280
Pearson Correlation	2	-0.074	-.393**	-.359**	.497**	-0.053	-0.086	-0.100	-.635**
Sig. (2-tailed)		0.491	0.001	0.001	0.000	0.625	0.424	0.353	0.000
N		89	67	89	89	89	89	89	72
Pearson Correlation	3	-.609**	.339**	0.026	.734**	.232**	.520**	.501**	-.631**
Sig. (2-tailed)		0.000	0.000	0.694	0.000	0.000	0.000	0.000	0.000
N		231	216	231	231	231	224	226	222
Pearson Correlation	4	-.261**	0.141	0.056	.491**	.228*	.359**	.341**	-.409**
Sig. (2-tailed)		0.004	0.131	0.540	0.000	0.012	0.000	0.000	0.000
N		121	116	121	121	121	121	121	119
Pearson Correlation	5	-0.151	0.251	-.410**	.779**	-0.220	0.261	0.261	-.471**
Sig. (2-tailed)		0.307	0.100	0.004	0.000	0.133	0.073	0.074	0.001
N		48	44	48	48	48	48	48	48
Pearson Correlation	6	0.149	0.573	0.509	0.625	0.539	.858*	.773*	.871*
Sig. (2-tailed)		0.750	0.179	0.244	0.133	0.212	0.014	0.042	0.011
N		7	7	7	7	7	7	7	7

References

Ahmed, M., Rappenglück, B., Das, S., Chellam, S. (2001). Source apportionment of volatile organic compounds, CO, SO_2 and trace metals in a complex urban atmosphere. *Environmental Advances, 6, 100127.* https://doi.org/10.1016/j.envadv.2021.100127

Amos, H. M., Jacob, D. J., Holmes, C. D., Fisher, J. A., Wang, Q., Yantosca, R. M., Corbitt, E. S., Galarneau, E., Rutter, A. P., Gustin, M. S., Steffen, A., Schauer, J. J., Graydon, J. A., Louis, V. L. St., Talbot, R. W., Edgerton, E. S., Zhang, Y., and Sunderland, E. M. (2012). Gas-particle partitioning of atmospheric Hg(II) and its effect on global mercury deposition. *Atmos. Chem. Phys., 12, 591–603*. https://doi.org/10.5194/acp-12-591-2012

Bank, M. (2020). The mercury science-policy interface: History, evolution and progress of the Minamata Convention. *Science of the Total Environment 722, 137832.* https://doi.org/10.1016/j.scitotenv.2020.137832

Branco, J.M., Hingst-Zaher, E., Jordan-Ward., R., Dillon, D., Siegrist, J., Fischer, J.D., Schiesari, L., von Hippel, F.A., Buck, C. L. (2022). Interrelationships among feather mercury content, body condition and feather corticosterone in a Neotropical migratory bird, the Purple Martin (*Progne subis subis*). *Environmental Pollution 314, 120284* https://doi.org/10.1016/j.envpol.2022.120284

Castro, P.J., Kellö, V., Cernušák, I., Dibble, T.S. (2022). Together, Not Separately, OH and O_3 Oxidize $Hg^{(0)}$ to $Hg^{(II)}$ in the Atmosphere. *The Journal of Physical Chemistry A 126 (44), 8266-8279* DOI: 10.1021/acs.jpca.2c04364

Calvert, J.G., Chatfield, R.B., Delany, A.C., Martel, E.A. (1985). Evidence for short SO_2 lifetimes in the atmosphere; An in-situ measurement of atmospheric SO_2 lifetime using cosmic ray produced ^{38}S. *Atmos.Environ.19(7), 1205-1206).* https://doi.org/10.1016/0004-6981(85)90205-7

Calvert, J. G., Lindberg, S. E. (2005). Mechanisms of mercury removal by O3 and OH in the atmosphere. *Atmos.Environ.39, 3355–3367*. https://doi.org/10.1016/j.atmosenv.2005.01.055

Coburn, S., Dix, B., Edgerton, E., Holmes, C. D., Kinnison, D., Liang, Q., ter Schure, A., Wang, S., and Volkamer, R. (2016). Mercury oxidation from bromine chemistry in the free troposphere over the southeastern US, *Atmos. Chem. Phys., 16, 3743–3760.* https://doi.org/10.5194/acp-16-3743-2016

Derry, E.J. (senior thesis forthcoming in spring 2023) Events of elevated oxidized atmospheric mercury at Storm Peak Laboratory.

Driscoll, C. T., Mason, R. P., Chan, H. M., Jacob, D. J., & Pirrone, N. (2013). Mercury as a global pollutant: Sources, pathways, and effects. *Environmental Science & Technology,47(10), 4967-4983.* doi:10.1021/es305071v

Faïn, X., Obrist, D., Hallar, A. G., McCubbin, I., Rahn, T.(2009). High levels of reactive gaseous mercury observed at a high elevation research laboratory in the Rocky Mountains. *Atmos.Chem.Phys.9, 8049–8060.* https://doi.org/10.5194/acp-9-8049-2009

Gingerich, D.B., Zhao, Y., Mauter, M.S. (2019). Environmentally significant shifts in trace element emissions from coal plants complying with the 1990 Clean Air Act Amendments. *Energy Policy 132, 1206-1215.* https://doi.org/10.1016/j.enpol.2019.07.003

Glasow, R., Bobrowski, N., Kern, C. (2009). The effects of volcanic eruptions on atmospheric chemistry. *Chemical Geology, 263(1-4), 131-142.* https://doi.org/10.1016/j.chemgeo.2008.08.020

Gratz, L., Jaffe, D.A., Hee, J.R. (2014). Causes of increasing ozone and decreasing carbon monoxide in springtime at the Mt. Bachelor Observatory from 2004 to 2013. *Atmos. Environment. 109, 323-330.* https://doi.org/10.1016/j.atmosenv.2014.05.076

Gratz, L, E. (2021). Ambient mercury observations in wildfire plumes at two Western U.S. sites using an improved dual-channel measurement system. *AGU fall meeting, Abstract.*

Gratz, L.E., Hallar, A.G., Hirshorn, N.S., Lyman, S.N., Elgiar, T., Hoch, N., Volkamer, R. Observations of trace gases and aerosols in biomass burning plumes at a high-elevation observatory in the Intermountain West during the 2021 wildfire season. Submitted to the 103rd Annual Meeting of the American Meteorological Society (AMS), 25th Conference on Atmospheric Chemistry, Denver, CO, January 2023.

Gratz, L., Lyman S., Volkamer, R., Hallar, A.G. (2022) Mercury oxidation pathways in a continental atmosphere: High temporal resolution measurements of mercury and oxidants at Storm Peak Laboratory. Project Description.

Gustin, M. S., Amos, H. M., Huang, J., Miller, M. B., Heidecorn, K. (2015). Measuring and modeling mercury in the atmosphere: a critical review. *Atmos.Chem. Phys. 15, 5697–5713*. https://doi.org/10.5194/acp-15-5697-2015

Harada, M. (1995). Minamata Disease: Methylmercury Poisoning in Japan Caused by Environmental Pollution, *Critical Reviews in Toxicology, 25:1, 1-24,* DOI: 10.3109/10408449509089885

Hoch, N.W. (senior thesis forthcoming in spring 2023) The effect of three upwind coal-fired power plants on air mass composition at a high elevation laboratory in the U.S. Intermountain West.

Jaffe, D.A., Lyman, S., Amos, H.M., Gustin, M.S., Huang, J., Selin, N.E., Levin, L., ter Schure, A., Mason, R.P., Talbot, R., Rutter, A., Finley, B., Jaeglé, L., Shah, V., McClure, C., Ambrose, J., Gratz, L., Lindberg, S., Weiss-Penzias, P., Sheu, G.R., Feddersen, D., Horvat, M., Dastoor, A., Hynes, A.J., Mao, H., Sonke, J.E., Slemr, F., Fisher, J.A. Ebinghaus, R., Zhang, Y., Edwards, G. (2014). Progress on understanding atmospheric mercury hampered by uncertain measurements. *Environmental Science & Technology 48 (13), 7204-7206.*DOI: 10.1021/es5026432

LaCount. M.D., Haeuber, R.A., Macy, T.R., Murray, B.A. (2021). Reducing power sector emissions under the 1990 Clean Air Act Amendments: A retrospective on 30 years of program development and implementation. *Atmos.Environ.245, 118012.* https://doi.org/10.1016/j.atmosenv.2020.118012

Lyman, S. N., Cheng, I., Gratz, L. E., Weiss-Penzias, P., & Zhang, L. (2020). An updated review of atmospheric mercury. *The Science of the Total Environment,707, 135575.* doi:10.1016/j.scitotenv. 2019.135575

Lyman, S. N., Jaffe, D. A. (2012). Elemental and oxidized mercury in the upper troposphere and lower stratosphere. *Nat.Geosci.5,114–117*. Doi: 10.1038/ngeo1353

Mesowest: Weather conditions for STORM. https://mesowest.utah.edu/cgi-bin/droman/meso_base_dyn.cgi?stn=STORM. Date accessed July 1, 2022.

NOAA. (2022). HYSPLIT Tutorial. https://www.ready.noaa.gov/documents/Tutorial/html/index.html. Accessed 10 November 2022.

NOAA. (2022). HYSPLIT Clustering Equations. https://www.ready.noaa.gov/documents/Tutorial/html/traj_cluseqn.html. Accessed 11 November 2022.

Obrist, D., Hallar, A. G., McCubbin, I., Stephens, B. B., and Rahn, T. (2008). Atmospheric mercury concentrations at Storm Peak Laboratory in the Rocky Mountains: Evidence for long-range transport from Asia, boundary layer contributions, and plant mercury uptake, *Atmos. Environ., 42, 7579–7589,* doi:10.1016/j.atmosenv.2008.06.051, 2008.

Obrist, D., Kirk, J.L., Zhang, L., Sunderland, E.M., Jiskra, M., Selin, N.E. (2018). A review of global environmental mercury processes in response to human and natural perturbations: Changes of emissions, climate, and land use. *Ambio* 47, 116–140. https://doi.org/10.1007/s13280-017-1004-9

Pan, L., Carmichael, G.R., Adhikary, B., Tang, T., Streets, D., Woo, J.H., Friedli, H.R., Radke, L.F. (2008). A regional analysis of the fate and transport of mercury in East Asia and an assessment of major uncertainties. *Atmospheric Environment, 42.6, 1144-1159.* https://doi.org/10.1016/j.atmosenv.2007.10.045

Pavithra, K. G., SundarRajan, P., Kumar S., Rangasamy (2023). Mercury sources, contaminations, mercury cycle, detection and treatment techniques: *A review, Chemosphere, Volume 312, Part 1, 2023, 137314, ISSN 0045-6535,* https://doi.org/10.1016/j.chemosphere.2022.137314.

Shah, V., Jacob, D.J., Thackray, C.P., Wang, W., Sunderland, E.M., Dibble, T.S., Saiz-Lopez, A., Černušák, I., Kellö, V., Castro, P.J., Wu, R., Wang C. (2021). Improved Mechanistic Model of the Atmospheric Redox Chemistry of Mercury. *Environmental Science & Technology 55 (21), 14445-14456* DOI: 10.1021/acs.est.1c03160

Stein, A.F., Draxler, R.R, Rolph, G.D., Stunder, B.J.B., Cohen, M.D., and Ngan, F. (2015). NOAA's HYSPLIT atmospheric transport and dispersion modeling system. *Bull. Amer. Meteor. Soc., 96, 2059-2077*. http://dx.doi.org/10.1175/BAMS-D-14-00110.1

Swartzendruber, P. C.,Jaffe, D. A.,Prestbo, E. M.,Weiss-Penzias, P.,Selin, N. E.,Park, R.,Jacob, D. J.,Strode, S., Jaeglé, L.(2006),Observations of reactive gaseous mercury in the free troposphere at the Mount Bachelor Observatory, *J. Geophys. Res.,111, D24301*, doi:10.1029/2006JD007415.

Timonen, H., Ambrose, J. L., Jaffe, D. A. (2013). Oxidation of elemental mercury in marine airmasses. *Atmos. Chem. Phys., 13, 2827–2836.* doi:10.5194/acp-13-2827-2013.

UN environment program: Minamata convention of -https://www.mercuryconvention.org/en. Date accessed 10 November 2022.

Wang, S., Schmidt, J.A., Baidar, S., Coburn, S., Dix, B., Koenig, T.K., Apel, E., Bowdalo, D., Campos, T.L., Eloranta, E., Evans, M.J., DiGangi, J.P., Zondlo, M.A., Gao, R.S., Haggerty, J.A., Hall, S.R., Hornbrook, R.S., Jacob, D., Morley, B., Pierce, B., Reeves, M., Romashkin, P., ter Schure, A., Volkamer, R. (2015). Active and widespread halogen chemistry in the tropical and subtropical free troposphere. PNAS 112 (30) 9281-9286. https://doi.org/10.1073/pnas.1505142112

World Health Organization. (2017). Mercury and health, https://www.who.int/news-room/fact-sheets/detail/mercury-and-health. Accessed 3 December 2022.

Zwecker, Z. (2021). Observations of ambient mercury from Storm Peak Laboratory using an improved dual-channel measurement system. Senior Thesis.